T.C.
YEDİTEPE UNIVERSITY
INSTITUTE OF HEALTH SCIENCES
DEPARTMENT OF MEDICAL PHYSICS

CALCULATION OF DETECTOR SPECIFIC OUTPUT CORRECTION FACTORS BASED ON IAEA-AAPM TRS-483 FOR 6 MV FLAT / UNFLAT PHOTON BEAMS AND COMPARISON WITH LITERATURE

BURCU HIZ TEMİZER

MASTER THESIS

İSTANBUL-2022

T.C.
YEDİTEPE UNIVERSITY
INSTITUTE OF HEALTH SCIENCES
DEPARTMENT OF MEDICAL PHYSICS

CALCULATION OF DETECTOR SPECIFIC OUTPUT CORRECTION FACTORS BASED ON IAEA-AAPM TRS-483 FOR 6 MV FLAT / UNFLAT PHOTON BEAMS AND COMPARISON WITH LITERATURE

BURCU HIZ TEMİZER

MASTER THESIS

SUPERVISOR
PROF. DR. ŞERİFE İPEK KARAASLAN

CO-SUPERVISOR
DR.CEMİLE CEYLAN

İSTANBUL-2022

THESIS APPROVAL FORM

Institute : Yeditepe University Institute of Health Sciences

Programme : Medical Physics

Title of the Thesis : Calculation of Detector Specific Output Correction Factors based on IAEA-AAPM TRS-483 for 6 MV Flat / Unflat Photon Beams and Comparison With Literature

Owner of the Thesis : Burcu Hız Temizer

Examination Date : 17.01.2022

This study have approved as a Master Thesis in regard to content and quality by the Jury.

	Title, Name-Surname (Institution)
Chair of the Jury & Supervisor	Prof. Dr. Ş. İpek KARAASLAN Yeditepe University
Co-Supervisor	Dr. Cemile Ceylan Yeditepe University
Member/Examiner:	Prof. Dr. Hilal ACAR DEMİR Istanbul Medipol University
Member/Examiner:	Prof. Dr. Mehmet Burçin ÜNLÜ Bogazici University
Member/Examiner:	Dr. Andaç HAMAMCI Yeditepe University

APPROVAL

This thesis has been deemed by the jury in accordance with the relevant articles of Yeditepe University Graduate Education and Examinations Regulation and has been approved by Administrative Board of Institute with decision dated 20.01.2022 and numbered 2022/01-47.

Prof. Dr. Bayram YILMAZ

Director of Institute of Health Sciences

DECLARATION

I hereby declare that this thesis is my own work and that, to the best of my knowledge and belief, it contains no material previously published or written by another person nor material which has been accepted for the award of any other degree except where due acknowledgment has been made in the text.

17/01/2022

BURCU HIZ TEMİZER

DEDICATION

To my Family with love

ACKNOWLEDGEMENTS

First and foremost, I would like to thank my esteemed advisor, Prof. Dr. Şerife İpek Karaaslan, who accepted me to this program, gave me the opportunity to become a student years later, opened the doors of the academic world, and gave me the chance to write these lines today, believing that everyone can succeed, regardless of age and time, if given the opportunity.

I would like to thank my valuable instructors, Dr. Cemile Ceylan and Dr. Türkay Toklu, for their endless patience and effort towards me during my Dissertation process, despite their hectic work schedules.

In addition, I am sincerely grateful to my co-advisor Dr. Cemile Ceylan who gave me all types of support and took measurements with me for days till the mornings at the Istanbul Oncology Hospital during the experiments of my Dissertation, despite her own troubles. As a medical physicist, your love of research and passion for learning has lit and inspired me on this path.

I am thankful to Dr. Alper Özkan, Medical Physicist Şermin Berrin Yilmaz, Dr. Songül Karaçam, Dr. Salih Gürdallı, Dr. Sümeyra Can, Medical Physicist Boran Güngör, Medical Physicist Serpil Yöndem İnal, Medical Physicist Zeynep Özen, Medical Physicist Cihan Şahin for providing the equipment I required for my Dissertation investigations.

Finally, I would also like to thank my husband, my only love and life partner Emrah Temizer, who has been with me from the beginning to the end of this trip and has never lost faith in my success. I am glad you are in my life.

TABLE OF CONTENTS

THESIS APPROVAL FORM ii
DECLARATION iii
DEDICATION iv
ACKNOWLEDGEMENTS v
LIST OF TABLES ix
LIST OF SYMBOLS AND ABBREVIATIONS xiii
ABSTRACT xv
ÖZET xvi
1. INTRODUCTION AND PURPOSE 1
2. GENERAL INFORMATION AND LITERATURE REVIEW 4
2.1. Ionizing Radiation 4
2.2. X-Ray Production 5
2.3. Ionizing Radiation Interactions with Tissue 5
2.3.1. Photon Interactions with Tissue 5
2.3.2. Particle Interactions with Tissue 7
2.4. Radiation Therapy 8
2.4.1. Historical Advancements at Radiation Therapy 9
2.4.2. Linear Accelerator (LINAC) 12
2.4.3. Radiation Therapy Techniques 15
2.4.3.1. 3DCRT 15
2.4.3.2. IMRT 16
2.4.3.3. VMAT 19
2.4.3.4. IGRT 19
2.4.3.5. Small Field Applications (SRS/SRT/SBRT) 21
2.4.4. Other Treatment Systems at Radiation Therapy 24
2.4.4.1. Tomotherapy 25
2.4.4.2. CyberKnife 25
2.4.4.3. IORT 25

2.5. Photon Dosimetry of Linac-Based Stereotactic Applications (SRS/SRT/SBRT) 26
2.5.1. Flattening-Filter-Free Beams vs Flattening Filter Beams.....26
2.5.2. Introduction to Small Field Dosimetry 28
2.5.3. Physics of Small Field Dosimetry 29
2.5.3.1. Beam-related Issues 29
2.5.3.2 Detector-related Issues.....31
2.5.3.3 Effect of Geometric Field size and Radiation Field size 33
2.5.3.4. Reference Dosimetry (Alfonso Formalism) 33
2.5.3.5. Relative Dosimetry 35
2.5.3.6. Detectors used for Reference and Relative Dosimetry in Linac-based Small Field measurements.....36
2.5.3.7. Impact of Small Field Dosimetry over Beam Modelling at Treatment Planning Systems 39
2.5.3.8. Brief Description of TPS Dose Calculation Algorithms 40
3. MATERIALS AND METHODS.....42
3.1 Overview to Equipments 42
3.2 Intermediate field size calculation with Daisy Chain technique for IBA CC13.....44
3.3 Detector position in water phantom measurements.....45
3.4 Measurements with IBA Smart Scan Water Phantom.....46
3.5 Output Factor measurements for 7 active detector 47
3.6 EBT 3 Gafchromic Film Measurements with RW3 Solid Phantom.....47
3.7 Scanning Procedure of EBT 3 Gafchromic Films 48
3.8 ImageJ analysis software for the convertion of Optical Density values to absorbed dose at EBT3 Gafchromic Film 49
3.8.1 Calibration Curve.....49
3.8.2 Dose Film readings 50
4. RESULTS 51
4.1 6 WFF Photon beam 51
4.1.1 Measurements and Calculations 51
4.1.2 Graphs.....57
4.2 6 FFF Photon beam.....58

4.2.1 Measurements and Calculations 58
4.2.2 Graphs 64
4.3 T-test Statistical Analysis and Percentage Variation 65
5. DISCUSSION AND CONCLUSION 68
6. REFERENCES 76
7. CURRICULUM VITAE 82

LIST OF TABLES

Table 2.1 Photon interaction probabilities in water per 100 photons.....7

Table 3.1 Characteristics of the detectors used for measurements 42

Table 4.1.1.1 3 times measured IBA CC13 ion chamber electrometer readings (cGy) for intermediate field sizes (4 cm x 4 cm) and reference Field sizes (10 cm x 10 cm) and corrected values applied polarization correction. 51

Table 4.1.1.2 The mean values of 3 times electrometer readings (cGy) for each detector per field sizes. Polarizatian corrections are applied for the ion chambers. 52

Table 4.1.1.3 Mean values of EBT3 Gafchromic film readings per field size read 3 times (5 scans each) and normalized to 500 MU. 53

Table 4.1.1.4 Detector Output Factors calculated with Daisy Chain Technique (OF_{det}) for each field size 54

Table 4.1.1.5 Gafchromic Film (EBT3) Output Factors for each field sizes(Ω_{EBT3}).....55

Table 4.1.1.6 Detector specific Output Correctipn Factors for each field size $kQclin,\ Qmsrfclin,\ fmsr$ 56

Table 4.1.2.1 3 times measured IBA CC13 ion chamber electrometer readings (cGy) for intermediate field sizes (4 cm x 4 cm) and reference Field sizes (10 cm x 10 cm) and corrected values applied polarization correction. 58

Table 4.1.2.2 The mean values of 3 times electrometer readings (cGy) for each detector per field sizes. Polarizatian corrections are applied for the ion chambers...59

Table 4.1.2.3 Mean values of EBT3 Gafchromic film readings per field size read 3 times (5 scans each) and normalized to 500 MU. 60

Table 4.1.2.4 Detector Output Factors calculated with Daisy Chain Technique (OF_{det}) for each field size 61

Table 4.1.2.5 Gafchromic Film (EBT3) Output Factors for each field sizes(Ω_{EBT3}).....62

Table 4.1.2.6 Detector specific Output Correctipn Factors for each field size $kQclin,\ Qmsrfclin,\ fmsr$ 63

Table 4.3.1 P values obtained as a result of 6 WFF and 6 FFF Photon Beam comparions for each detector 65

Table 4.3.2 Percentage variation of our 6 WFF results from TRS-483 values for each detector 66

Table 4.3.3 Percentage variation of our 6 FFF results from TRS-483 values for each detector..... 67

LIST OF FIGURES

Figure 2.1 Electromagnetic Radiation (Spectrum) 4

Figure 2.2 Possibility of Interactions Observed in Radiation Oncology 5

Figure 2.3 Chronology of equipment used radiation therapy since the discovery of X-rays by Wilhelm Conrad Roentgen 10

Figure 2.4 Percent Deep Dose (PDD) curve over depth for various EBRT techniques ..11

Figure 2.5 LINAC Basic schema 12

Figure 2.6 A shows the Linac treatment head in photon mode (with flattening filter) B shows the Linac treatment head in electron mode (with scattering foil) 14

Figure 2.7 Different MLCs 15

Figure 2.8 MLC shaping using BEV 16

Figure 2.9 3DCRT (homogeneous dose distribution) versus IMRT (inhomogeneous dose distribution-better OAR protection) 17

Figure 2.10 3DCRT and IMRT isodose curves for the prostate cancer case 17

Figure 2.11 Static MLC (Step-and-Shoot) 18

Figure 2.12 Dynamic MLC (sliding window) 18

Figure 2.13 VMAT technique utilized in Head-and-Neck treatment 19

Figure 2.14 Negative Ratio, B: Suitable Ratio, C: Best Ratio 20

Figure 2.15 The 3D visualization of the tumor localization 21

Figure 2.16 Non-invasive SRS treatment 22

Figure 2.17 The local control success at Lung Tumor with SBRT 22

Figure 2.18 The SBRT treatment success after 6 weeks and 5 months intervals at liver malignancies 23

Figure 2.19 Lateral profile of 6 MV FFF and 10 MV FFF beams showing the reduction of dose distribution with respect to distance 27

Figure 2.20 Difference in lateral beam profile of WFF and FFF photon beams 28

Figure 2.21 The photon beam area diameters where equilibrium is attained and lost for various energies 30

Figure 2.22 Blocking of the main source by collimator at small fields 31

Figure 2.23 The Volume Averaging effect induced by the Ion Chamber length/cm used for Small Field Dosimetry 32
Figure 2.24 (a) Geometric field size is equal to irradiation field size (FWHM)
(b) Geometric field size < irradiation field size
(c) Geometric field size << irradiation field size (Widening of area, overlapping of Penumbra) 34
Figure 2.25 Air-filled cavity chamber design 38
Figure 2.26 Sample Flow-chart to be followed for beam-modeling and treatment planning 40
Figure 3.1 IBA Smart Scan Water Phantom 43
Figure 3.2 Ashland EBT 3 Gafchromic film (LOT 01142102) 43
Figure 3.3 Detector orientation inside water phantom 46
Figure 3.4 Irradiation of Gafchromic films 48
Figure 3.5 Scanning process of Gafchromic films 49
Figure 3.6 6 WFF Calibration Curve 50
Figure 4.1.2.1 6 WFF Photon beam Output Factor plots against field sizes 57
Figure 4.1.2.2 6 WFF Photon beam Output Correction Factor plots against field sizes 57
Figure 4.2.2.1 6 FFF Photon beam Output Factor plots against field sizes 64
Figure 4.2.2.2 6 FFF Photon beam Output Correction Factor plots against field sizes 64
Figure 5.1.a Ion Chambers Output correction factors at 10 cm depth for 6 WFF 69
Figure 5.1.b Solid-State Detectors Output correction factors at 10 cm depth for 6 WFF 69
Figure 5.2.a Ion Chambers Output correction factors at 10 cm depth for 6 FFF 70
Figure 5.2.b Solid-State detectors Output correction factors at 10 cm depth for 6 FFF 70

LIST OF SYMBOLS AND ABBREVIATIONS

AAPM	American Association of Physicists in Medicine
TG	Task Group
IAEA	International Atom Energy Agency
TRS	Technical Report Series
TCP	Tumor Control Probability
NTCP	Normal Tissue Complexity Probability
DVH	Dose-Volume Histogram
OAR	Organ at Risk
3DCRT	3 Dimensional Conformal Radiotherapy
IMRT	Intensity-Modulated Radiotherapy
VMAT	Volumetric Arc Therapy
IMAT	Intensity-modulated Arc Therapy
SRT	Stereotactic Radiation Therapy
SRS	Stereotactic Radiosurgery
SBRT	Stereotactic Body Radiation Therapy
IGRT	Image-guided radiation therapy
IORT	Intra-operative Radiotherapy
EBRT	External Beam Radiotherapy
LINAC	Linear Accelerator
MLC	Multi-leaf Collimator
FFF	Flattening-filter free
WFF	with Flattening Filter
PDD or %dd	Percent depth dose
SSD	Source to surface distance
SAD	Source to axis distance
TAR	Tissue-Air Ratio
TMR	Tissue Maximum Ratio

TPS	Treatment Planning System
TLD	Thermoluminescent dosimeter
MOSFET	Metal–oxide–semiconductor field-effect transistor
MU	Monitor Unit
EPID	Electronic Portal Imaging Device
PTV	Planned Target Volume
GTV	Gross Target Volume
CTV	Clinical Target Volume
CBCT	Cone-beam Computed Tomography
ABC	Active Breath Control
CT	Computed Tomography
MRI	Magnetic Resonance Imaging
PET	Positron Emission Tomography
FWHM	Full width half maximum
EPOM	Effective point of measurement
CAX	Central axis
LCPE	Lateral charged particle equilibrium

ABSTRACT

Hız Temizer, B. (2022). Calculation of Detector Specific Output Correction Factors Based on IAEA-AAPM TRS-483 for 6 MV Flat / Unflat Photon Beams and Comparison With Literature. Yeditepe University, Institute of Health Science, Department of Medical Physics, MSc thesis, İstanbul.

In the TRS-483 recommendations, output correction factors to be applied in small fields are specified as a single value for each detector and field size, regardless of the Linac model, collimation, or filtering difference. For small fields where LCPE is lost, dosimetric measurements are seriously affected by the presence of the detector used in the absorbed dose measurements resulting in problems like Volume Averaging and Perturbation effects. Since Scp values are used in the treatment MU value calculations, if the Correction Factors due to the detector differences are entered into the TPS incompletely, the dose calculations are incorrect in the plans where small fields such as SRS, SRT, SBRT are used frequently. In our study, correction factors for 7 different detectors and 9 different field sizes (0.5, 1.0, 2.0, 2.5, 3, 3.5, 4.0, 4.5, 5.0 cm^2) were calculated using the experimental method and their compatibility with the correction factors specific to the detectors specified in the literature was investigated. 6 MV WFF and FFF photon output factors for CC01, CC04, Extradin A16, Pinpoint 3D, microDiamond, Edge and SRS Diode were calculated with Daisy Chain method using the intermediate field. Correction factors were found for each detector using the calculated field output factor for the EBT3 film. All measurements were performed on the Versa HD system. The field size of 4 x 4 cm^2 and a CC13 ion chamber were used for intermediate-field calculations. It was observed that ion chambers are under-response in field sizes smaller than 3 cm^2 and need a larger correction factor, whereas solid-state detectors are over-response, and need a relatively smaller correction factor than ion chambers. The percent variation between the correction factors for the two energies 6 WFF / 6 FFF was found to be a maximum of 2% for both ion chambers and solid detectors at field sizes of 2 cm^2 and larger. There was a significant difference between the correction factors found for all detectors we used in our study for both energies in the field sizes smaller than 2 cm^2.

Keywords: Correction Factors, Small Field Dosimetry, TRS-483

ÖZET

Hız Temizer, B. (2022). Flat/Unflat 6 MV Foton Küçük Alan Output Faktör Ölçümlerinde Farklı Detektörler İçin TRS 483 Tavsiyesinde Düzeltme Faktörlerinin Belirlenmesi ve Karşılaştırılması. Yeditepe Üniversitesi Sağlık Bilimleri Enstitüsü, Medikal Fizik ABD, Master tezi, İstanbul.

TRS-483 önerilerinde küçük alanlarda uygulanacak output düzeltme faktörleri Linac model farkı, kolimasyon ve filtrelasyon farkı olmaksızın her detektör ve alan boyutu için tek değer olarak belirtilmiştir. LCPE'nin kaybolduğu küçük alanlar için soğurulan doz ölçümlerinde kullanılan detektörün varlığından dolayı dozimetrik ölçümler ciddi şekilde etkilenmekte; hacim ortalaması, pertürbasyon etkileri gibi sorunlar oluşmaktadır. Tedavi MU değeri hesaplamalarında Scp değerleri kullanıldığından dedektör farklılığından kaynaklı Düzeltme Faktörlerinin TPS'e yanlış ya da eksik girilmesi durumunda SRS, SRT, SBRT gibi küçük alanların sıkça kullanıldığı planlarda doz hesaplamaları yanlış olmaktadır. Çalışmamızda 7 farklı detektör ve 9 farklı alan boyutu (0.5, 1.0, 2.0, 2.5, 3, 3.5, 4.0, 4.5, 5.0 cm^2) için düzeltme faktörleri deneysel yöntem kullanılarak hesaplandı ve literatürde belirtilen detektörlere özgü düzeltme faktörleri ile uygunluğu araştırıldı. CC01, CC04, Extradin A16, Pinpoint 3D, microDiamond, Edge ve Diode SRS için 6 MV WFF ve FFF foton output faktörleri Daisy Chain yöntemi ile orta alan kullanılarak hesaplandı. EBT3 film için hesaplanan field output faktörü kullanılarak her bir detektör için detektöre özgü düzeltme faktörleri bulundu. Tüm ölçümler Versa HD cihazında gerçekleştirildi. Orta Alan hesaplamaları için 4 x 4 cm^2 alan boyutu ve CC13 iyon odası kullanıldı. Iyon odalarının 3 cm^2'den küçük alan boyutlarında under-response olduğu ve bu sebepten daha büyük düzeltme faktörüne ihtiyaç duyduğu, katı hal detektörlerin ise over-response olduğu ve daha küçük düzeltme faktörüne ihtiyaç duyduğu gözlemlendi. Ayrıca, iki farklı enerji 6 WFF / 6 FFF için bulduğumuz düzeltme faktörleri arasında ki yüzde sapma 2 cm^2 ve daha büyük alan boyutlarında hem iyon odalari hem de katı hal detektörler için maksimum % 2 olarak bulundu. 2 cm^2'den daha küçük alan boyutlarına gidildikçe ise iki enerji için de kullandığımız tüm detektörler için bulunan düzeltme faktörleri arasında anlamlı fark oluştuğu gözlemlendi.

Anahtar Kelimeler : Düzeltme Faktörleri, Küçük Alan Dozimetresi, TRS-483

1. INTRODUCTION AND PURPOSE

Radiation Therapy is the treatment method that damages the DNA to prevent the growth and spreading of the tumor cells within the body using Ionization Radiation. Its goal is safely delivering the prescribed dose to tumor cells while limiting the radiation to healthy tissues in the surrounding area. TCP (Tumor control probability) and NTCP (Normal Tissue Complication Probability) models are the indications of the success rates of the planned treatment. The outcome of these models are displayed in Dose-Volume Histograms (DVH) to evaluate target and OAR (Organs at Risk) doses (1). S_{cp} readings are used to calculate treatment MU values. Dose calculations will be erroneous in treatment plans when small fields such as SRS, SBRT, and SRT are commonly employed if output correction factors are incorrectly or incompletely supplied owing to detector differences. Since imperfect dosimetry measurements can have major impacts such as significantly higher doses or potentially fatal clinical results for patients, it is crucial to comprehend the physics and limitations involved. Guidelines, such as IAEA TRS-398 (2), AAPM TG-51 (3), IAEA TRS-483 (4), AAPM TG-155 (5) are available to guide the application of accurate dosimetry measurements under different conditions to avoid dose measurement errors (4).

Due to the technological breakthrough of treatment techniques IMRT (Intensity-Modulated Radiation Therapy), VMAT (Volumetric Arc Therapy), SRT (Stereotactic Radiotherapy), SRS (Stereotactic Radiosurgery), SBRT (Stereotactic Body Radiation Therapy), higher dose fractionations in daily clinical use have become standard procedures. With these kinds of techniques, it is now possible to deliver high doses to nonconventional fields (< 3 x 3 cm^2) denoted as “small fields”. On the other hand, when dealing with small fields, accurate dosimetry measurements can be significantly more challenging compared to conventional fields (large fields). These physical dosimetry issues related to small fields are clearly emphasized at IAEA TRS-483 Code of Practice (CoP), alongside the implementations and protocols that should be taken into consideration when dealing with relative and reference dosimetry for external beam photon radiation therapy (6).

Various detectors with different physical properties suitable for the small field dosimetry have been produced by manufacturers (7). When the area of interest is small field, suitable detectors should have minimal energy dependence to produce high SNR with a noise reduction. The wall material and electrode material of the detectors should be suitable for small field measurements not to cause the Volume Averaging Effect.

The assumption that the ratio of absorbed dose to measured detector readings for larger field size where LCPE achieved, is almost equal, is also not valid for small field dosimetry measurements. Due to the Volume Averaging and Perturbation Effect of the detector employed at measurements, the measured doses must be multiplied by a coefficient depending on the characteristics of the detector used to calculate the absorbed dose. In the literature, this coefficient is known as the output correction factor, and it is provided in detailed lists in the IAEA TRS-483 Code of Practice (CoP) for different operating energies (6 and 10 MV photon beams), detectors, and devices (Linac, CyberKnife machines, Tomotherapy machines, Gamma Knife) (4,8).

An extensive number of investigations have been conducted and are continuing by many researchers around the world to avoid erroneous dose measurements caused by the small field dosimetry challenges. In this dissertation, our goal is to calculate the output correction factors for 2 energies (6 MV WFF and FFF photon beams), 7 different detectors (IBA CC01, IBA CC04, SI Extradin A16, PTW Pinpoint 3D, PTW microDiamond, SN Edge, and PTW Diode SRS) and 9 different field sizes (0.5, 0.8, 1, 2, 2.5, 3, 3.5, 4, 5 cm^2) using the experimental method, and benchmark our findings with the published parameters for each detector in the TRS-483 Code of Practice. All measurements were collected using an Elekta Versa HD Linac system equipped with an Agility 160-Leaf MLC (Multi-Leaf Collimator). In our study, the Daisy Chain technique described in the literature is used to determine the relative output factors and to minimize the Volume Averaging Effect caused by the detector in small fields. This technique also uses three different field sizes: the reference field (10 x 10 cm^2), the 4 x 4 cm^2 intermediate field, and the clinical field size.

This thesis has three aims. 1) To calculate the detector-specific output correction factors for the detectors and field sizes we used in our study and to compare the results with the literature, 2) To calculate output correction factors for detectors and field sizes not

included in TRS-483 CoP and contributing to the literature, 3) To examine the dose-response of the detectors for two different energies (6 WFF / 6FFF).

2. GENERAL INFORMATION AND LITERATURE REVIEW

2.1. Ionizing Radiation

The transmission of energy between matters is known as Radiation. Ionizing radiation has the potential to disintegrate orbital electrons directly or indirectly by transferring their energy to those electrons. It is divided into two types: Ionizing Electromagnetic Radiation (X-Rays and γ-Rays (indirect effect)) and Ionizing Particle Radiation (electrons, beta particles, alpha particles, ions, protons (direct effect)). Electromagnetic Radiation is classified as Ionizing Radiation and Non-Ionizing Radiation based on its wavelength, frequency, and energy as shown in Figure 2.1. Since Wilhelm Conrad Roentgen's discovery of X-Rays in 1895, Ionizing Radiation has been used in medicine for both therapy and imaging (9, 10).

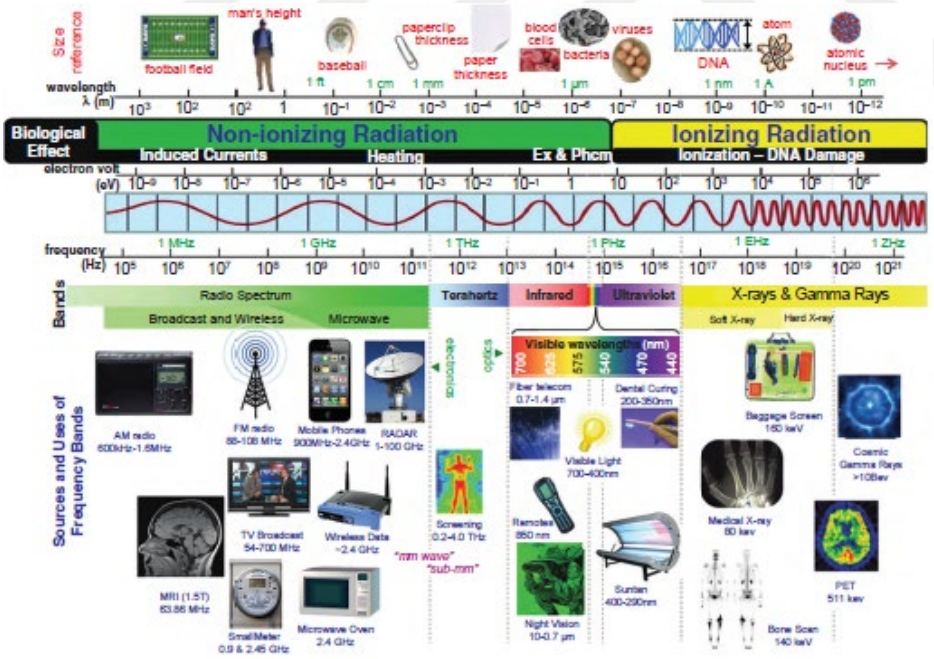

Figure 2.1 Electromagnetic Radiation (Spectrum) (10)

Photons and electrons, which are frequently used in clinical radiotherapy, are obtained by accelerating electrons in Linear Accelerators. Photons can also be obtained

through radioisotopes, which become stable by emitting Gamma Rays during the splitting of atomic nuclei. In addition, heavy particles, such as ions and alpha, are also used in treatments.

2.2. X-Ray Production

The X-Ray tube is of a high-pressure tube design. By applying a high voltage between the anode and the cathode, the high-atomic-number tungsten material that serves as the cathode is heated, resulting in the elimination of electrons from the cathode. Bremsstrahlung X-Rays or Characteristic X-Rays are produced when these electrons contact the anode (made of a different material such as copper). Although the working principle of Linac is the same as the x-ray tube, there are differences which will be detailed in further sections (1, 9).

2.3. Ionizing Radiation Interactions with Tissue

2.3.1. Photon Interactions with Tissue

As a result of the interaction of photons with tissue, the below-mentioned interactions occur depending on photon energy and the atomic number of tissue (10, 11, 12). Figure 2.2 and Table 2.1 depict three different interactions observed in Radiation Oncology applications based on energy ranges (11, 13).

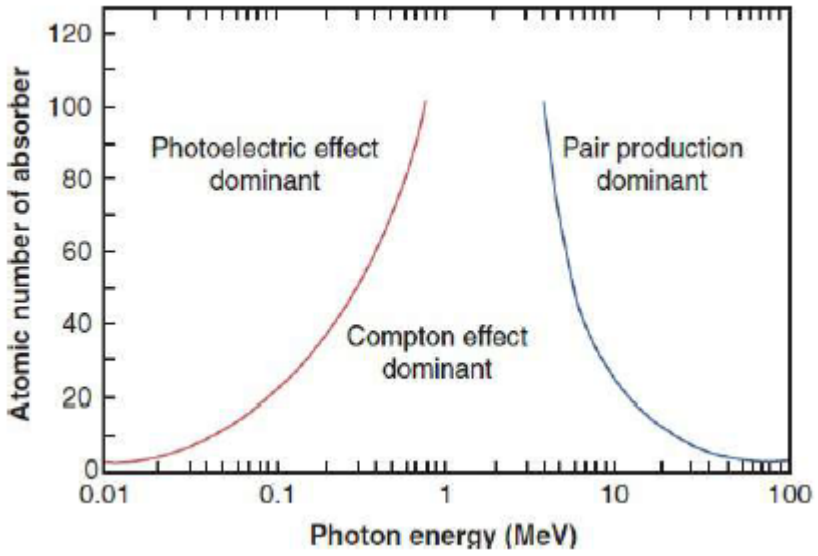

Figure 2.2 Possibility of Interactions Observed in Radiation Oncology (13)

1) In Rayleigh scattering, the energy of the incident photon is not large enough to knock the electrons out of their orbits. Therefore; the incoming photon energy is transferred to the whole atom and causes orbital electrons to vibrate. Afterwards, a photon is released with the same energy as the incoming photon, but in a different angle. Since it occurs at low energies, it is likely to occur in applications such as mammography.
2) Compton scattering occurs between the incident photon and the electrons in the outer orbit. As a result, although the electron in its outer orbit is removed, the incident photon's entire energy is shared between the scattered electron and the Compton photon, and they are dispersed at various angles depending on the incident photon's energy. The greater the energy of the incoming photon, the more likely it is for Compton scattering to occur. For this reason, it can be said that radiation is the dominant interaction in Oncology applications.
3) The photoelectric effect occurs when the kinetic energy of a low-energy photon is equivalent or higher than the orbital binding energy when interacting with a material having a K orbital binding energy of 0.5 keV, such as soft-tissue. As a result, an electron whose kinetic energy is the difference between the energy of the incident photon and the binding energy (K, L, M, N orbital binding energies), is knocked out of the atom. This atom is in an ionized state. The vacant orbital is filled with a lower energy orbital electron. During this transition, either the characteristic x-ray is emitted or the Auger electron is released.
4) Pair production is not an observable interaction in Diagnostic Imaging and Radiation Oncology. The incoming photon interacts with the atomic nucleus, causing a positron and an electron to be knocked out of the atom. For a positron-electron pair to form as a result of pair production, the incoming photon energy must be at least 1.02 MeV and above. It interacts with other atoms on the emitted electron and positron path by ionization, excitation, and Bremsstrahlung x-ray. As the positron kinetic energy ends, it is destroyed by combining with a free electron and radiates its energy as two gamma rays of 511 KeV in opposite directions. This phenomenon is called positron annihilation.

5) Photodisintegration should be taken into consideration when determining linear accelerator room shielding, due to the high energy used in Radiation Oncology. Photons with an energy of more than 10 MV interact with the atomic nucleus, resulting in neutron emission.

Table 2.1 Photon interaction probabilities in water per 100 photons

Energy Level (MeV)	Photoelectric Effect	Compton Effect	Pair Production
0.010	95	5	0
0.026	50	50	0
0.060	7	93	0
0.150	0	100	0
4.000	0	94	6
10.00	0	77	23
24.00	0	50	50
100.00	0	16	84

2.3.2. Particle Interactions with Tissue

Interactions of a lightly charged particle (electron): Ionized particle radiation is also utilized in Radiation Oncology treatments. When lightly charged particles such as electrons pass through a medium like soft tissue or water, they interact with the electric field of the electron or nucleus (Coulomb forces) in 3 ways; ionization, excitation, or Bremsstrahlung x-rays. If the energy of the incoming electron is greater than the binding energy of the orbital electron, the orbital electron is knocked out of the atom and an ion pair is formed. This ion pair continues to make secondary ionizations (Delta rays) on its way. This phenomenon is called ionization. If the energy of the incoming electron is not greater than the binding energy of the orbital electron, the electron moves to an upper orbital (further from the nucleus), and then returns to its original orbit. This interaction is called excitation. As a result of these interactions, energy is absorbed by the environment. Finally, if the energy of the incoming electron is large enough, it interacts with the electric field of the atomic nucleus and transfers its energy to the medium as the Bremsstrahlung x-ray (10, 12).

Interactions of a heavily charged particle (ion or alpha): Since specific ionization is directly proportional to the square of the charge, heavily charged particles such as alphas or ions cause a large amount of ionization along their path. Before they lose all their kinetic energy and stop; their maximal energy is absorbed by the environment at a point known as Bragg Peak. The Bragg Peak characteristic of heavily charged particles plays an essential role in Radiation Oncology treatments (10, 12).

2.4. Radiation Therapy

Radiation Therapy is a therapeutic approach that uses ionizing radiation to damage the DNA to prevent tumor cells from growing and spreading throughout the body. The primary purpose is to deliver the recommended dose to tumor cells while preserving the surrounding healthy tissues, known as OAR (Organ at Risk) as much as possible (1).

The depth and size of the tumor, i.e. the target to be treated, defines the kind of ionizing radiation and hence the energy needed for therapy. While photons are used to treat thick areas such as the gastrointestinal tract or lung cancers, electron therapy is used to treat malignancies that are on or near the skin's surface, such as lip tumors (1, 9).

Ionizing radiation was initially used in medical applications in 1896, and radiotherapy usage in cancer treatment began shortly after. Today's radiotherapy applications are classified into three categories based on their purpose, application period, and type (1, 9).

- Radiotherapy based on its purpose can be examined in 4 subgroups.

1. Curative Therapy: It is concerned in increasing the life expectancy of patients by killing as many cancer cells as possible. It is the first approach in early-stage cancer treatments.
2. Palliative Treatment: It focuses on increasing the patient's quality of life and life expectancy by reducing pain and symptoms in advanced malignancies that have metastasized.
3. Prophylactic Treatment: Its main scope is to stop the spread and repetition of the tumor.

4. Whole Body Irradiation: This is the procedure performed before stem cell transplantation. The goal is to clear the way for stem cells by eliminating leukemia cells.

- Radiotherapy is examined in 3 subgroups based on its application period.

1. Adjuvant Radiotherapy: The first procedure used in this approach is not radiotherapy; instead, radiotherapy is used after other treatments, such as surgical excision of malignant tissue.
2. Neo-Adjuvant Radiotherapy: The primary method in this approach is radiotherapy.
3. Radio-chemotherapy: In this approach, radiotherapy and chemotherapy are applied simultaneously.

- Finally, radiotherapy is divided into 2, based on its type.

1. External Beam Radiotherapy (EBRT): It is a procedure in which ionizing radiation is delivered to the area to be treated with linear accelerator devices (generally due to Co-60 and intraoperative devices).
2. Internal Radiotherapy: It is a method of applying ionizing radiation to the region to be treated using radioisotopes that are either temporarily or permanently implanted on the area to be treated, such as Brachytherapy.

2.4.1. Historical Advancements at Radiation Therapy

Figure 2.3 shows the technological developments in radiotherapy from the discovery of x-rays to the present day, depending on the ionizing radiation used (13). A very short time after the discovery of x-ray, a breast cancer patient was treated for the first time by applying x-ray. In the beginning of the 20^{th} century, treatments for stomach cancer, skin cancer, and leukemia began to be tried. In 1902, the first x-ray dosimeter studies were carried out using a chromo-radiometer. Following the discovery of the ion chambers in the middle of the 20^{th} century, in 1928, for the first time dosimetry measurements were carried out using the ion chamber. Before the high-energy radiotherapy devices, which are widely used in clinics

today, devices that produce low-energy x-rays were widely used. The first low-energy EBRT device was the Granz ray therapy device. Treatments were carried out using x-rays with an energy lower than 20 kV. Following this device, contact therapy devices that produce x-rays in the 40-50 kV range began to be used. Superficial therapy devices producing 50-150 kV x-ray and ortho-voltage therapy devices producing 150-500 kV energy are examples of low-energy radiotherapy devices used before today's advanced technologies (13, 14).

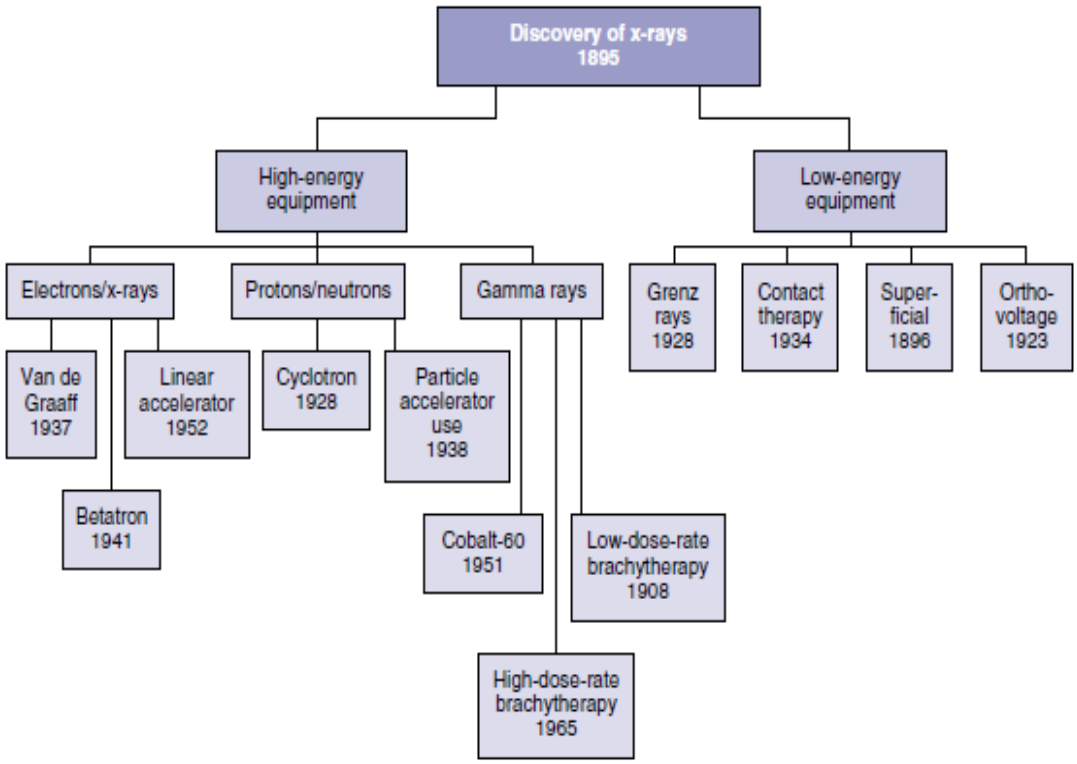

Figure 2.3 Chronology of equipment used in radiation therapy since the discovery of x-rays by Wilhelm Conrad Roentgen (13)

The most important feature of low-energy EBRT devices is that the depth of penetration is very low due to the rapid absorption of energy by the tissue, and therefore they can only be used in superficial tumor treatments. In the 1950's-1960's, the first clinical applications of EBRT devices, Co-60 and linac, which produce high-energy x-rays greater

than 1 MV, began to take place. Figure 2.4 (15, 14) shows the percent deep dose curve relative to the subcutaneous distance for low-energy EBRT devices and Co-60 devices. In the historical development, linac devices based on the working principle of accelerating the charged particles (electrons) created by eletron gun and hitting the target, are developed following the Co-60 devices. The working principle of linac will be explained in detail in the following section. After 1980, we see that advanced treatment techniques have been discovered and started to be applied. In 1982, IMRT technique, based on the principle of delivering the maximum dose to tumor cells while limiting the exposure of healthy tissue by using MLCs, started to be applied. In the following sections, conventional fraction techniques, such as IMRT / VMAT, and radiosurgery applications (SRS / SBRT), which is a high-dose treatment approach with less fraction, will be explained in detail. The desired doses are delivered to the target volume by using small fields. In these applications, the treatment time is shortened by using FFF beams, especially in SRS / SBRT. With specific radiation equipments like CyberKnife and Tomotherapy, as well as IGRT technology that enables real-time monitoring of the tumor's position and mobility, it is now feasible to properly administer the appropriate dosage to the target. These technologies demonstrate the current state of clinical practice.

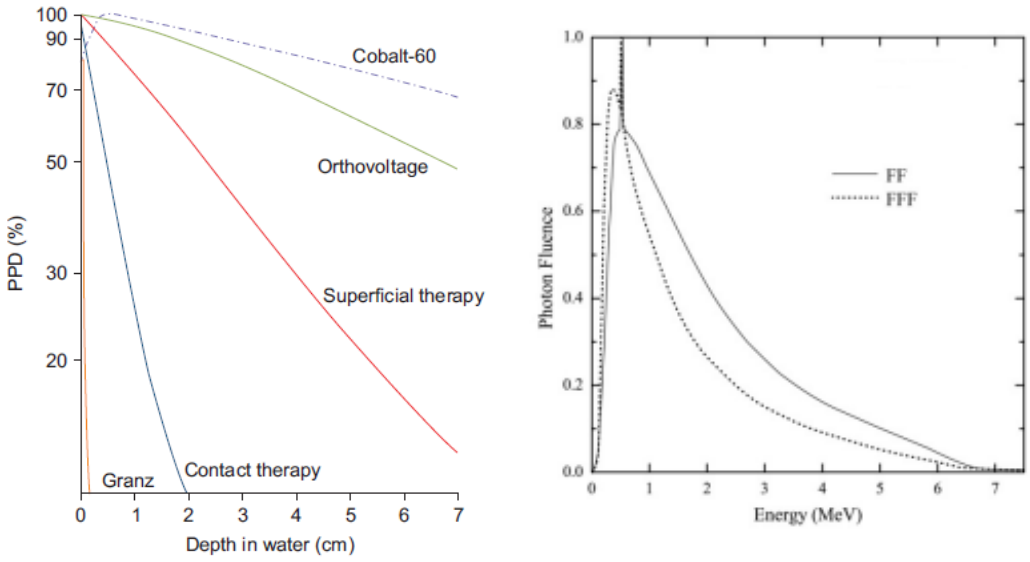

Figure 2.4 Percent deep dose (PDD) curve over depth for various EBRT at various energies (14, 15)

2.4.2. Linear accelerator (linac)

Charged particles such as electrons ejected from the electron gun are accelerated in an accelerator waveguide by high-frequency electromagnetic waves. As a result, high-energy electrons or x-rays are generated. Linac is a device that treats these high-energy electrons or x-rays by directing them to deep or surface located tumor cells. In linear accelerators (~3000 MHz) used in radiotherapy, electrons are accelerated by fixed or static electromagnetic waves (depending on the accelerator type) whose frequency corresponds to the microwave zone of the electromagnetic spectrum. The linac basic schema is shown in Figure 2.5 (1, 16).

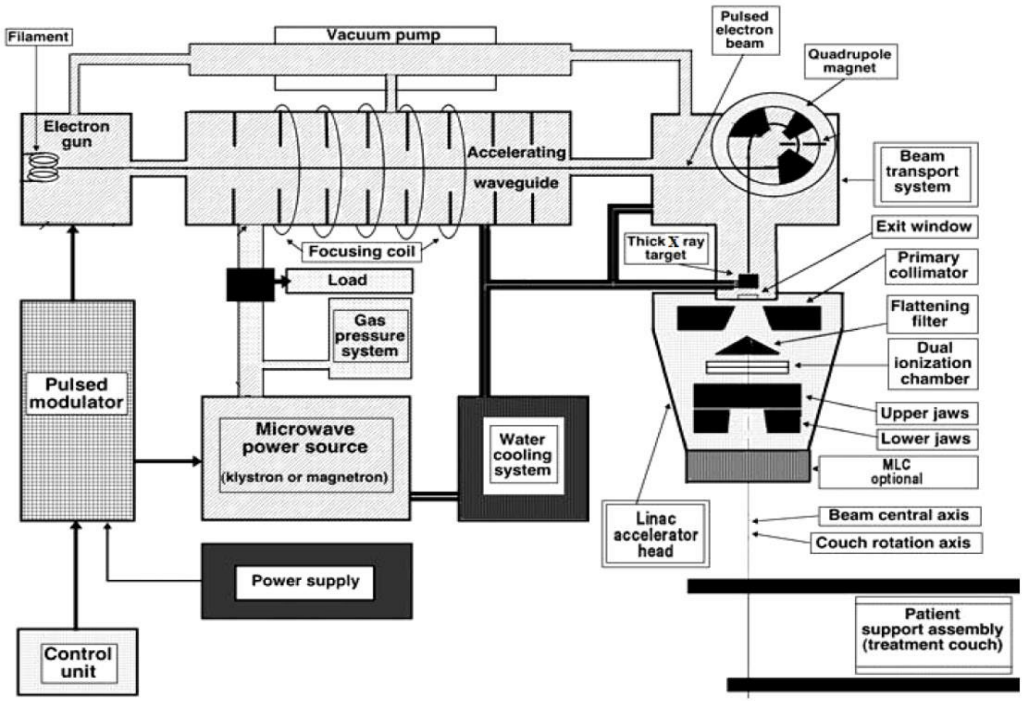

Figure 2.5 Linac basic schema (16)

Simply, the current is supplied to the modulator by the power supply. An adequately spaced microwave is produced using this shielded electric current. These microwaves are transmitted to both the electron gun and the magnetron or klystron at the same time.

Here, the klystron amplifies electrons with energies greater than 15 MeV, while the magnetron is responsible for generating waves at microwave frequency. The electron gun is an x-ray tube-like device, in which electrons produced by the heating of the filament, that acts as the cathode, reach the anode and are injected into the accelerator waveguide. At the same time, microwaves emanating from the magnetron or klystron are also sent into the accelerator waveguide. The accelerator waveguide is a vacuum tube consists of copper chambers. Microwaves produced by the magnetron and accelerated by the klystron generate vibrations at frequencies of 3000 Mhz in chambers and are transmitted to the center of the waveguide. Electrons with 50 keV energy injected from the electron gun into the accelerator waveguide are superimposed on these electromagnetic waves like someone surfing on the ocean, and are accelerated through each copper chamber. This process is called linear acceleration. The electrons are emitted by the accelerator waveguide in a form of a 3 mm pencil beam and are deflected 90 degrees or 270 degrees by the bending magnet before striking a high atomic number material such as tungsten inside the linac head (treatment head) to produce Bremsstrahlung x-rays or characteristic x-rays (photon mode) (9, 17).

Linear accelerators work in two different modes; photon mode and electron mode. In electron mode, the electrons directed by the bending magnet are directly focused on the treatment area with two different scattering foils (high and low atomic numbers) instead of hitting a target such as Tungsten. The aim is to obtain homogeneous dose distribution and a wide beam. In Radiation Oncology applications, photons in the range of about 4-23 MV obtained by hitting a target such as tungsten are used in the treatment of deeply located tumors, while electrons with an energy of about 5-21 MeV directed by the scattering foil are used in the treatment of superficial tumors (9, 12, 11). The detailed illustration of linac head is shown in Figure 2.6 (1).

Bremsstrahlung x-rays, which are formed as a result of the collision of electrons at MV energy levels hitting the target with a high atomic number, are poly-energetic. That means, there is an energy spectrum. Flattening filters are used to obtain a homogeneous x-ray distribution. In this way, homogeneous and symmetrical distribution of the incoming beam is ensured.

The incident beam's characteristics, such as homogeneity, symmetry, and dose rate, are assessed using an ion chamber placed below the flattening filter. These ion chambers have a working voltage range of 300-1000 V. The jaws are expanded to the size of the treatment field (from 0 x 0 to 40 x 40 cm^2) using secondary collimators, and the beam is supplied to the region of interest by collimating the beam. Besides the jaws, micro leaf collimators (MLCs) are used for the collimation of irregular treatment areas in advanced radiotherapy (9, 12, 17)

In small radiation field applications (advanced radiotherapy methods such as SRS/SRT/SBRT), which are also the subject of this dissertation, heterogeneous dose distributions are delivered to the treatment area at higher dose rates rather than homogeneous dose distributions. Due to the small target volumes in SRS techniques where high fraction doses are used, the desired dose is delivered to the target volume by using small fields, depending on the treatment delivery method chosen. Since the dose per fraction is high, FFF beams are frequently used in SRS / SBRT applications where a flattening filter is not used. FFF is more intense in the central axis and has a higher dose rate than FF beams, resulting in reduced treatment time (17). These treatment methods are referred to as "Flattening Filter Free". In this thesis, flattening filter-free beams will be denoted as FFF, while conventional beams using filters will be denoted as wFF.

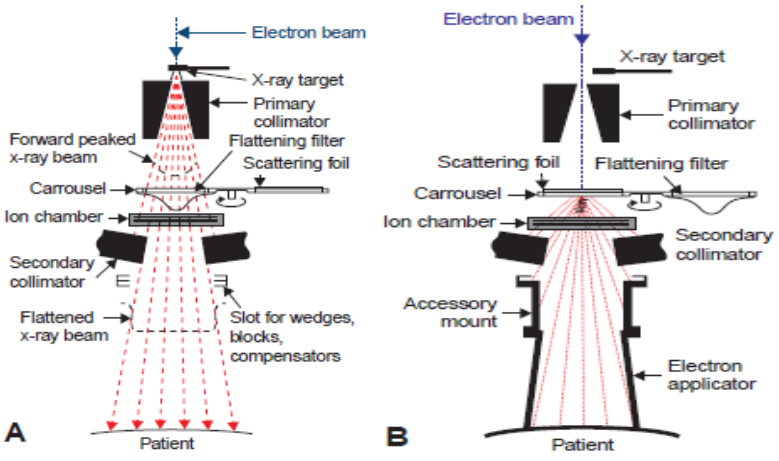

Figure 2.6 A shows the linac treatment head in photon mode (with flattening filter) B shows the linac treatment head in electron mode (with scattering foil) (17)

2.4.3. Radiation therapy techniques

2.4.3.1. 3DCRT

Conformal radiotherapy was invented in the early 1960's. With the development of tomography systems and advances in computer technology, it has become possible to show anatomy in three dimensions. The 3DCRT treatment technique has begun to take place in clinics as a result of advancements in tomography and immobilization techniques that ensure minimal movement of patients during treatment. As previously stated, the primary goal of radiotherapy is to guarantee that the healthy tissues neighboring the tumor are exposed to the least amount of radiation while providing the highest amount of radiation to the malignant tissue or organ. The volume intended to receive the dose prescribed by the Radiation Oncologist is referred to as the PTV (planning target volume). This is achieved with three-dimensional conformal irradiation. One of the most significant advancements in the 3DCRT method was the MLC (multi-leaf collimators) technology, which is built on high atomic number materials like Tungsten and allows irregular tumor areas to be treated by opening and shutting of leaves. Figure 2.7 illustrates different MLC devices (9).

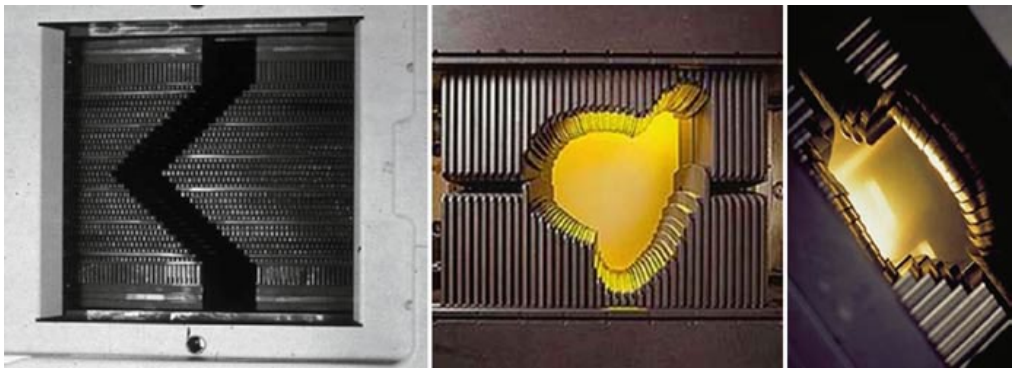

Figure 2.7 Different MLCs (9)

Beam eye view images (Figure 2.8) are used while the medical physicist creates the treatment plan in the clinic. In this way, the MLC leaves can be opened and closed manually by the user, in this way the beam is shaped to allow the best therapeutic rate to be achieved (18).

A 3DCRT method is a forward-planning-based approach in which the medical physicist plans how many areas and from which angle the beam will enter, beam weight (intensity), collimator/gantry angles, and energy values to obtain the optimum therapeutic ratio. Afterwards a uniform dose distribution is created by the system based on the entered beam parameters (19).

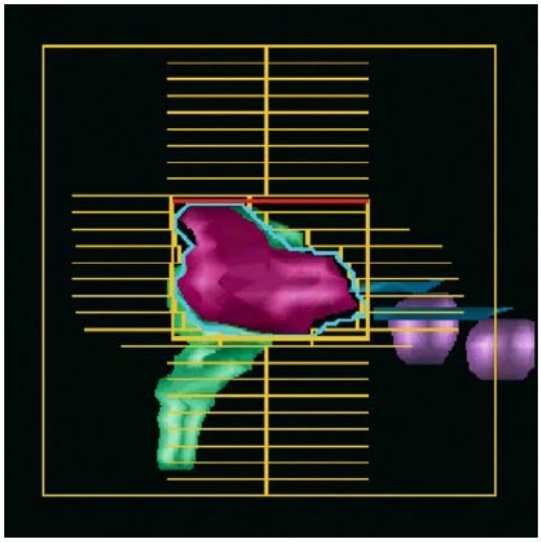

Figure 2.8 MLC shaping using BEV (18)

2.4.3.2. IMRT

The difference of the IMRT technique, which was developed in 1982 and is still widely used in clinics today, from 3DCRT is that it offers inverse planning. Non-uniform dose distribution and improved OAR protection can be obtained in this manner. Figure 2.9 depicts the distinction between 3DCRT and IMRT (19).

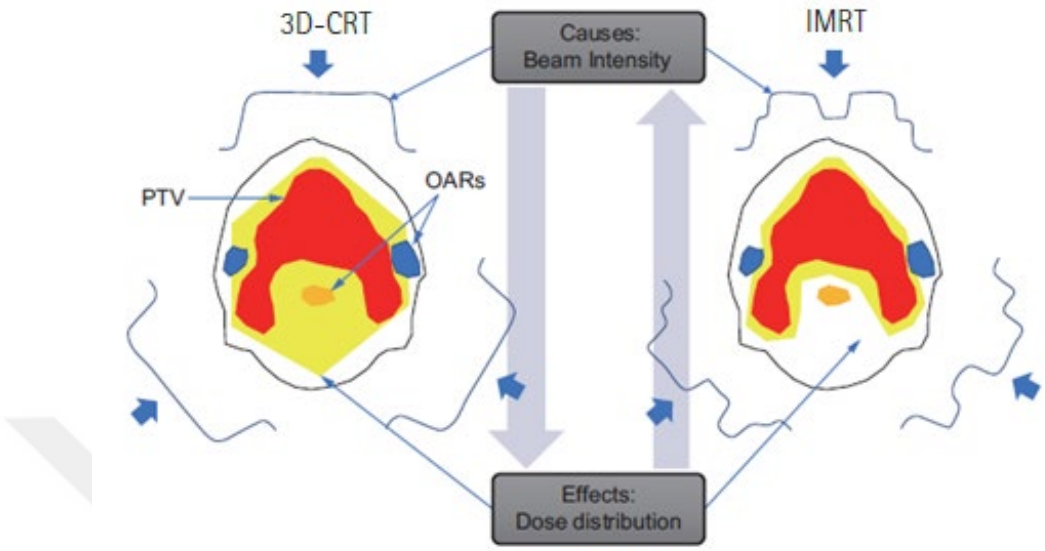

Figure 2.9 3DCRT (homogeneous dose distribution) versus IMRT (19)

While obtaining homogeneous dose distribution in 3DCRT, in IMRT, the irradiated target volume (PTV) and the doses of OARs (objectives and constraints) are planned by the medical physicist according to the prescribed dose. Then, beamlets/beam weights and intensity maps are created according to the objectives and constraints to be obtained inhomogeneous dose distributions by the system. Figure 2.10 shows the differences between 3DCRT and IMRT isodose curves, and it can be seen that OAR protection is better than 3DCRT when planning with the IMRT technique (20).

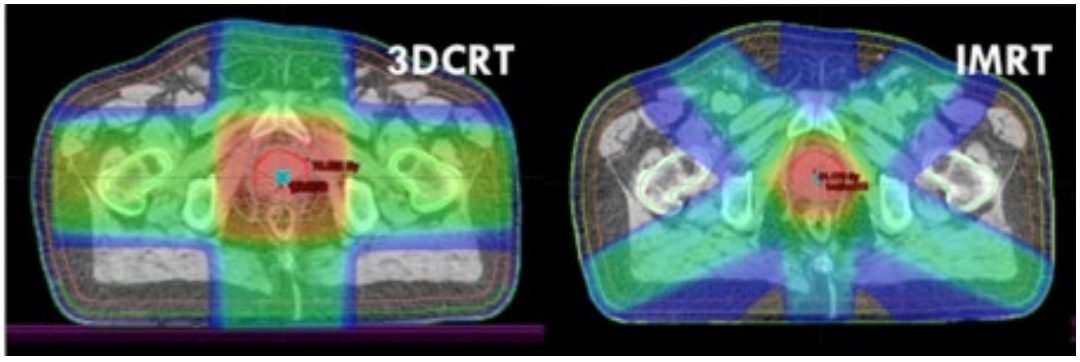

Figure 2.10 3DCRT and IMRT isodose curves (20)

The coming step after the composing of intensity maps based on beam properties is called leaf sequencing. In this optimization step, MLC leaves are opened by the system to cover the PTV according to the specified beam settings. Besides the advantages of IMRT, the drawback of this approach is that as the number of beamlets increase, so does the computer optimization time. In the IMRT technique, the intensity is adjusted in 3 different ways. 1) Static MLC (step-and-shoot), 2) Dynamic MLC (sliding window) and 3) VMAT. While the gantry and the MLC leaves are stationary in the step-and-shoot technique, irradiation is applied. MLC leaves only move when there is no irradiation. This approach allows both "forward" and "inverse" planning. Figure 2.11 depicts this approach (19, 21).

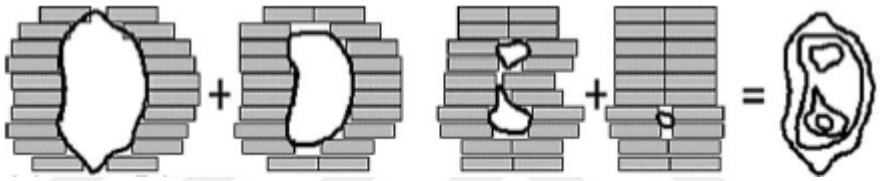

Figure 2.11 Static MLC (step-and-shoot) (19, 21)

In the second approach, dynamic MLC, the gantry is still fixed. Irradiation occurs concurrently with the movement of the MLC leaves. Only "inverse" planning can be done with this technique. This technique is shown in Figure 2.12 (19, 21).

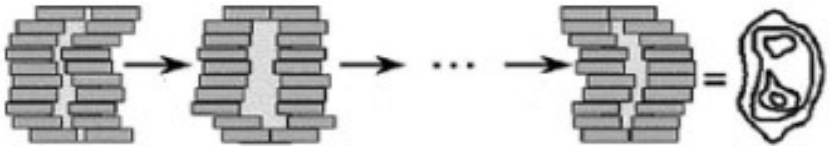

Figure 2.12 Dynamic MLC (sliding window) (19, 21)

The last method is the VMAT technique, in which the MLC leaves move and irradiate simultaneously with the gantry rotation shown in Figure 2.13 (1).

2.4.3.3. VMAT

IMAT technique, in which the gantry rotates during irradiation, has become possible by the invention of helical tomotherapy devices. The IMAT technique differs from the existing IMRT approach in that irradiation occurs throughout the gantry's continuous rotation. IMAT with fixed-dose rates developed into VMAT with continually changing dose rates during gantry rotation. Irradiation is conducted at different dose rates during various gantry rotation speeds in VMAT. This approach may be used to handle one 360-degree arc or two 180-degree arcs. Since VMAT treatment durations are shorter than IMRT treatments, total doses given to the patient is also less when compared. PTV coverage and OAR protection are far superior to 3DCRT and IMRT. The rapid completion of the treatment with techniques such as VMAT minimizes the errors that may occur during the treatment due to patient organ movement or patient movement, thus increasing the success rate of the treatment (1, 19)

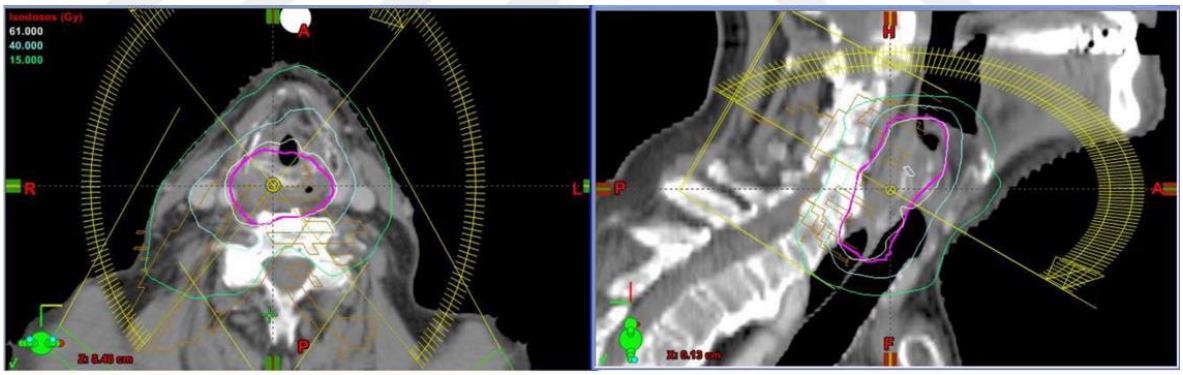

Figure 2.13 VMAT technique utilized in head-and-neck treatment (1)

2.4.3.4. IGRT

Image-guided radiotherapy is based on the comparison of the patient's images obtained before the treatment with the reference images obtained during the treatment period. The aim here is to minimize the errors that may occur between and within the fractions, and thus to increase the success of the treatment. Treatment success is expressed by therapeutic ratio. Therapeutic ratio refers to the ability to kill as many tumor cells as possible with the prescribed dose (raising TCP) while also protecting the surrounding healthy tissue to the

to the greatest extent possible (reducing of NTCP). Figure 2.14 shows therapeutic ratio graphs. In fractional treatments, setup errors may occur between or during treatments (22). Weight loss, tumor growth or shrinkage that may occur on the patient during the treatment, mechanical errors at the patient couch, technician errors are examples of setup errors between treatments (inter-fraction). Examples of setup errors that may occur during the treatment are respiratory movements, organ movements, patient movement errors (intra-fraction). All these errors affects the success of the treatment. With IGRT techniques, the patient is monitored throughout the treatment and these errors are minimized. With the images obtained with technologies such as EPID (MV imaging), CBCT (kV-kV imaging), on-rail imaging, ultrasound imaging, magnetic resonance imaging, it is possible to compare the patient's anatomy before treatment and during treatment, and so treatment plans are revised as needed (23, 24).

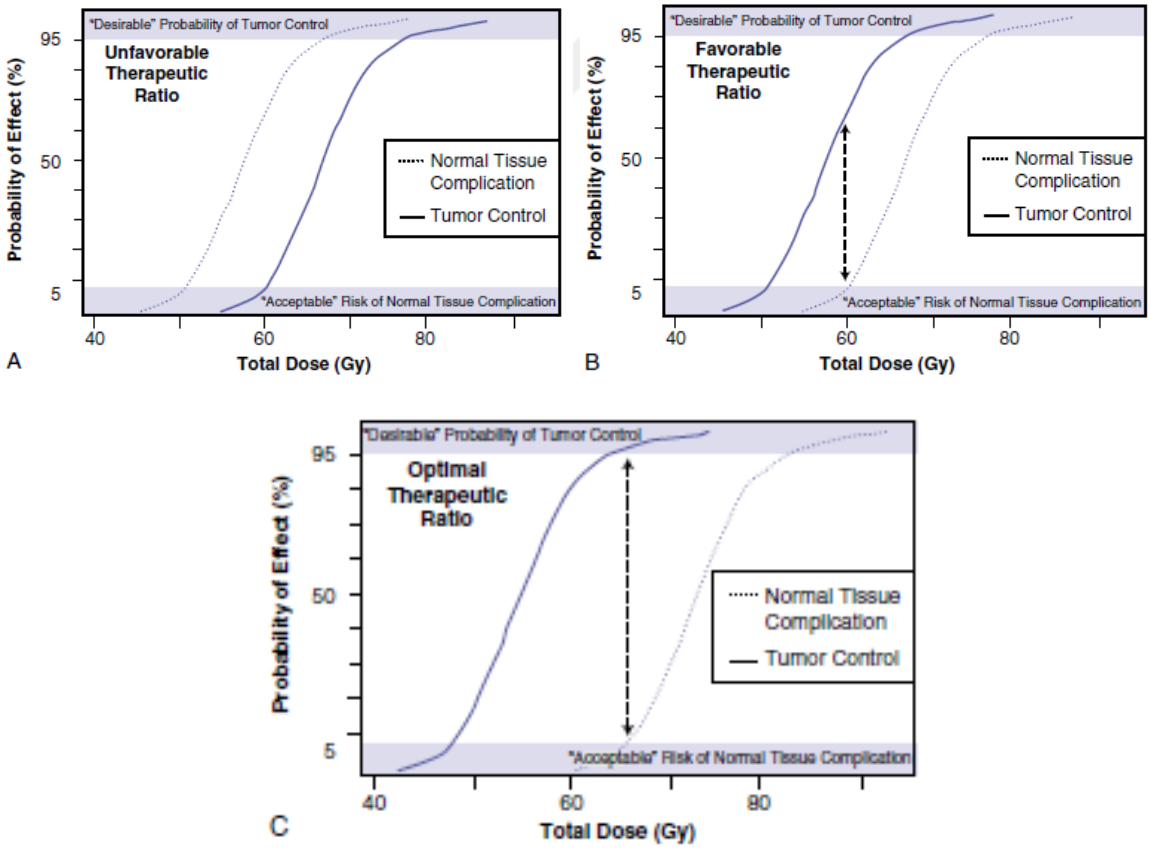

Figure 2.14 A: Negative ratio, B: Suitable ratio, C: Best ratio (22)

2.4.3.5. Small field applications (SRS/SRT/SBRT)

The Gamma Knife was the first SRS device created in 1951 for the treatment of brain malignancies and cerebral vascular disorders. This system developed by Lars Leksell was essentially a linear accelerator capable of directing gamma rays from diverse angles with the numerous Co-60 sources to a single point to be treated. Since the method is based on the treatment of a small field with very high dose rates, the patient's head was fixed with apparatus called frames in the early Gamma Knife systems (1, 24).

The region to be treated in stereotactic applications is not PTV, but rather main tumor (GTV) or CTV (clinical target volume) with very limited margin (setup errors). When treating GTV at large doses, it is aimed to protect the healthy tissues by a sharp dose-fall off at the point where GTV ends. For this reason, the immobilization of the patient's head is provided with apparatus called frame and frameless in intracranial applications (1, 24).

Apart from the special Gamma Knife device, extra-cranial and intra-cranial treatments are also possible with CyberKnife or conventional linac, which provide treatment with single fractions or multiple fractions. The 3D visualization of the location of the primary tumor in the x-y-z coordinate system and the ability to deliver the prescribed dose to the tumor volume accurately and precisely throughout the treatment period affect the success of the treatment (1, 24). Figure 2.15 shows the 3D visualization of the tumor localization (25).

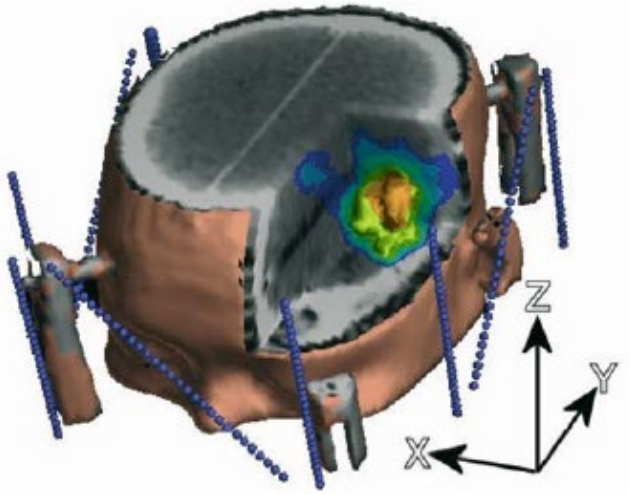

Figure 2.15 The 3D visualization of the tumor localization (25)

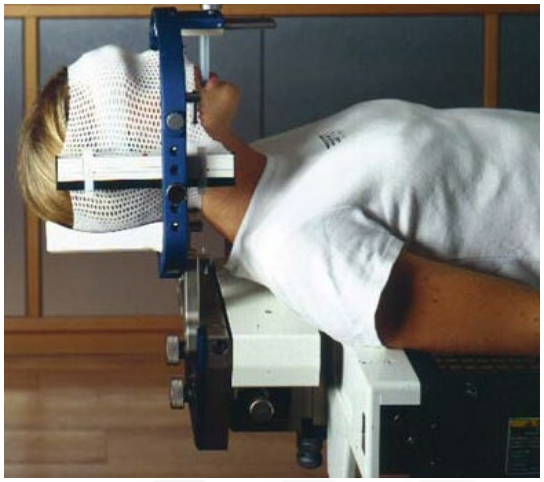

Figure 2.16 Non-invasive SRS treatment (25)

The difference of small field treatments from the treatment methods mentioned in the previous section is the fractionation scheme. SRS refers to intracranial small field lesion therapy with a single fraction and high dose rates. SRT refers to multi-fraction treatments again with high dose rates. Only intracranial anomalies and malignancies are treated with either method. SBRT, on the other hand, refers to small-field treatments administered at high dose rates of 1-5 fractions to extra-cranial areas such as the lung, lower/upper abdomen, and spinal cord (1, 24). Figure 2.17 illustrates the success of SBRT treatment compared pre-and post-situation of lung tumor (26). Figure 2.18 demonstrates the SBRT treatment success after 6 weeks and 5 months intervals at liver malignancies (26).

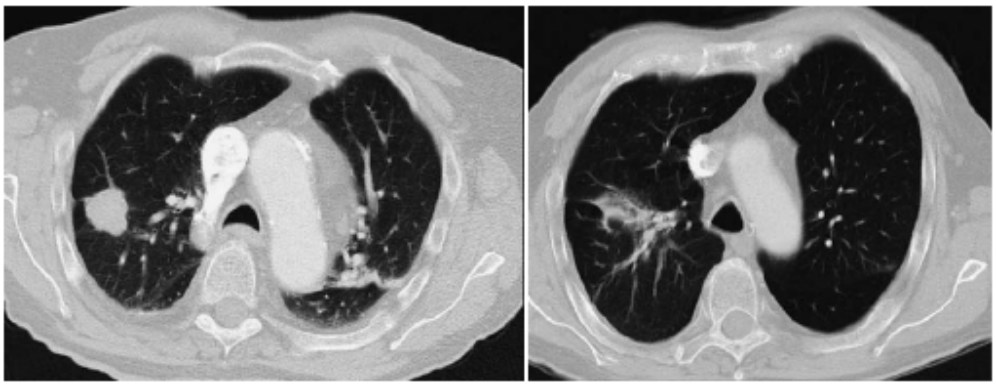

Figure 2.17 The local control success at lung tumor with SBRT (26)

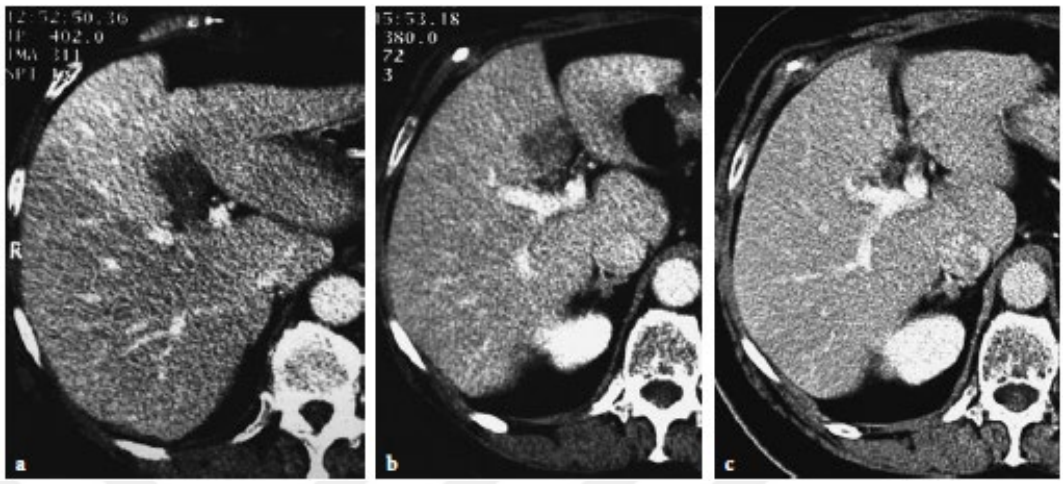

Figure 2.18 The SBRT treatment success after 6 weeks and 5 months intervals at liver malignancies (26)

It took a long time for the SBRT technique to be implemented in clinics compared to the SRS/SRT. For the SBRT procedure to be applied successfully, the patient must be immobilized and the same target must be irradiated at all times during the treatment (precise and accuracy). For this purpose, the location of the irradiated primary tumor is verified daily with IGRT methods throughout therapy. It is aimed to prevent erroneous irradiation and to minimize healthy tissue toxicity by comparing the reference images obtained with pre-treatment simulation devices and IGRT images. While the frame and frameless immobilization systems are used in SRS/SRT, vacuum-based solutions are also applied in SBRT. One of the biggest problems in extra-cranial regions is organ/tumor movement. To reduce tumor movement induced by breathing movements, abdominal compression, ABC (active breath control), and breath-holding methods are utilized. Each of these approaches has merits and downsides. However, the respiratory phases (inhalation/exhalation) may be seen, allowing tumor tracking and respiratory gating techniques with the ABC technique. Gerszten PC et al reported that SBRT therapy for the central nervous system (CNS)-spinal cord malignancies were successful at 90% over 500 patients with an average dosage of 20 Gy. In another research, Timmerman et al reported a 90% success rate for local control when SBRT was used in early-stage lung cancer patients in three fractions of 20 Gy each (malignancy smaller than 5 cm) (1, 24).

To obtain high rates of local control with small field treatments, all steps from small field dosimetry to beam modeling, high-accuracy imaging of the target volume (with CT, MR, and PET systems), simulation, immobilization of the patient throughout the treatment, treatment planning, treatment implementation, and beam delivery must be meticulously planned (1, 24). AAPM has published the TG-101 report detailing the methods to be followed for the use of correct procedures, methods, and systems in clinics for SBRT treatments (27).

The aim of small field treatments, as stated earlier, is to apply the extremely high doses with small fractions to the tumor volumes (high conformity), while also minimizing healthy organ damage by achieving a quick dose dropping at the border of GTV. Since high dose rates are applied at treatment of small fields, it is crucial to accurately calculate and transfer the beam-related parameters to the treatment planning systems to avoid secondary cancer issues following treatments. Beam modeling must be done with utmost precision to calculate accurate dose calculations by the dose calculation algorithms used in TPS. Small-field dosimetry, which is also the focus of this dissertation and its challenges which will be discussed in-depth in the coming parts, is still one of the most actively investigated radiotherapy subjects (1, 24).

2.4.4. Other treatment systems in radiation therapy

Dedicated radiotherapy devices employing X-band RF technology began to be developed in the 1990's as an alternative to the S-band RF technology linacs that are currently extensively utilized in clinics. In linac devices, the RF frequency operating range is 3000 MHz. CyberKnife, Tomotherapy, and IORT devices that employ X-band technology use higher RF frequencies. These treatments systems are advantageous in that they occupy a small space, have greater mobility, and are light. In the study conducted by Yujong K, Saitiniyazi S, Mayierjiang M, et al, performance evaluation of radiotherapy devices was evaluated according to RF frequencies (28). It has been stated that devices using X-band RF technology have disadvantages such as longitudinal non-linearity control in phase space, energy control, and photon bandwidth as well (10).

2.4.4.1. Tomotherapy

A tomotherapy system employs X-band RF technology. It is a linear accelerator capable of performing IMRT with 6 MV photons in helical or serial mode, in conjunction with tomography system technology. The magnetron generates electromagnetic waves, such as linacs. The tomography unit, which is an IGRT method, provides tumor inter or intra-fraction follow-up. The helical mode is the advancement of the patient table inside the gantry throughout the gantry's 360-degree continuous rotation. The beam is applied to the treatment field by opening and shutting 64 collimator leaves. SAD is 85 cm long, as opposed to linacs. In this manner, therapy may be administered at 850 cGy per minute dose rates (10).

2.4.4.2. CyberKnife

Another system using X-band RF technology is CyberKnife. With its real-time tumor tracking capabilities, it can perform small field treatments with excellent precision and accuracy, not only for SRS/SRT but also for SBRT applications. It is a 6 MV linac mounted on robotic arm-equipped non-isocentric therapy equipment (13, 24). In the study of Yu et al, it was reported that the treatment accuracy of the Cyberknife device is at submillimeter levels in spine malignancies (29).

2.4.4.3. IORT

IORT, which is a part of adjuvant treatment, is another method that uses X-band RF technology. IORT allows ionizing radiation to be delivered directly to the tumor site during the surgical procedure. When compared to linacs, it has the benefit of delivering the radiation once the tumor bed has been cleared during the operation, as opposed to a long-term fractionated therapy. During the operation, the surgeon can view the tumor and OAR. This improves the treatment's success rate (13). The rate of local control was shown to be high in early-stage breast malignancies, rectal and lung tumors, and pediatric illnesses in Goer A. et al's study (30). In the same study, a dose of 11.3 Gy in rectal cancer treatments was comparable to a dose of 20 Gy given with EBRT. It has been stated that the complication rate is low and the curative rate is high in applications under 15 Gy (30).

2.5. Photon dosimetry of linac-based stereotactic applications (SRS/SRT/SBRT)

2.5.1. Flattening-filter-free beams vs flattening filter beams

Photon treatments in linac devices are applied in two different ways: with flattening filter beams (such as 3DCRT applications) and flattening-filter-free beams (such as SRS/SRT/SBRT applications) (12).

Flattening filter beams (wFF): Electrons exiting the accelerator at near-light speed are deflected 90 or 270 degrees by bending magnets before striking a tungsten/copper mixture material with a high atomic number known as the flattening filter. As a result, two kinds of interactions occur. Primary interactions are caused by the photon source and secondary interactions are caused by electrons within the tissue which are scattered from the collimator or the linac device head. In the absence of a filter, the high-energy primary photon beam behaves more intensely in the central axis than in the lateral axis and provides forward penetration. When using the flattening filter, poly-energetic Bremsstrahlung x-rays (an energy spectrum with average energy) are created as a result of high-energy photons interacting with the filter. The filter produces a beam hardening effect by collecting low-energy x-rays in the center axis and decreasing their contribution to the beam's average energy. In this way, homogeneous dose distribution in both the central and lateral axis is achieved, that is, the beam is straightened (17, 31, 32, 16).

Flattening-filter- free beams (FFF): By using the advantage that the orientation and intensity of the primary photons are on the central axis and in the forward direction, heterogeneous beams are obtained (Figure 2.19 (32) and Figure 2.20 (12)). Since no filters are used in FFF treatments, the risk of secondary cancer that may occur in the post-treatment period is reduced as a result of the reduction of secondary interactions within the body caused by the electrons scattered from the linac head or the collimator. Treatments can be performed in a much shorter time at very high dose rates compared to wFF beams. Besides, the shortening of the treatment period reduces the risk of patient or organ or respiratory motion errors. Although FFF beams offer benefits over wFF beam treatments, dosimetry measurements and modeling of beam characteristics in treatment planning systems must be done with great precision and accuracy because treatments are delivered at extremely high

dose rates to very small treatment regions. Even if it varies depending on the manufacturer and device model, the maximum dose rate for 6 MV photon beams may be generalized to 1400 MHU/min and 2400 MHU/min for 10 MV photon beams (17, 31, 32, 16). The quality control tests that should be performed based on the treatment used, as well as the limitations that should be maintained, are defined in the TG-142 report (33).

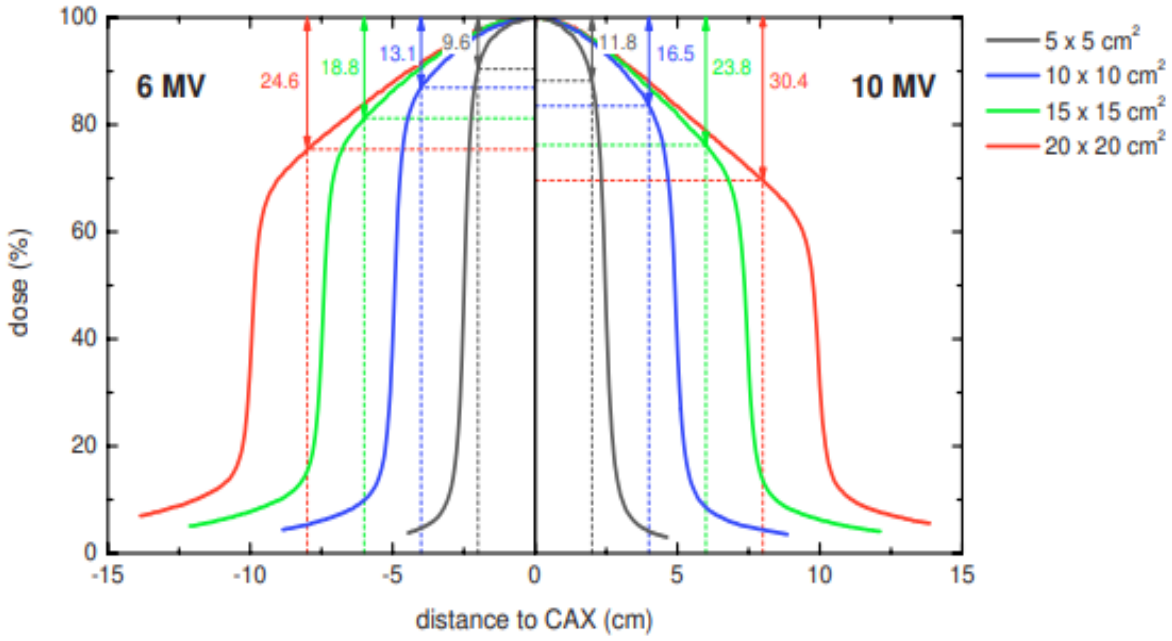

Figure 2.19 Lateral profile of 6 MV FFF and 10 MV FFF beams showing the reduction of dose distribution concerning distance (32)

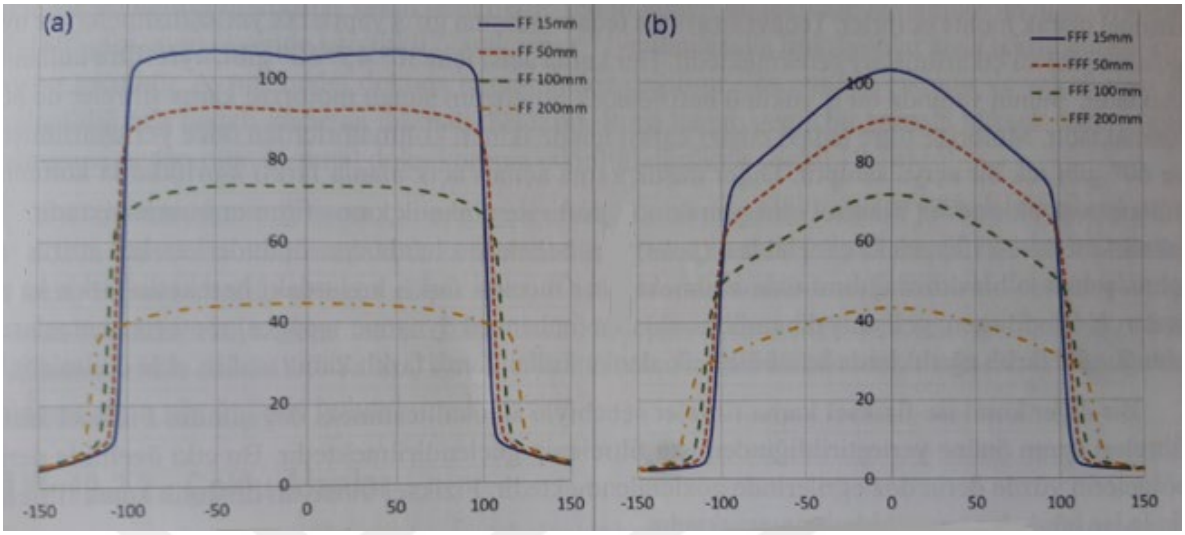

Figure 2.20 Difference in lateral beam profile of WFF and FFF photon beams (12)

2.5.2. Introduction to small field dosimetry

Dosimetry is all measurements and calculations to accurately represent the energy absorbed by a unit mass of an organ or tissue (17). Since high-energy photon treatments, such as SRS/SBRTdeals with very small fields less than 3 x 3 cm^2, small field dosimetry presents distinct challenges when compared to large field dosimetry, due to beam and detector associated factors. There are established recommendations for small field dosimetry measurements in the literature, such as TRS-483 (4) and AAPM TG-155 (5), as well as numerous studies and publications (4, 17, 5).

Since the human body is utilized as the basis for the absorbed dose measurements, the water phantom is employed as the medium, and the absorbed dose measurements calculations are in the water (12, 31). According to ICRU-91 guidelines, 6 MV photon beam dose measurements include % dd (for SSD calibrations) or TPR/ TMR (for SAD calibrations) in the z-axis, lateral profiles (crossline in the x-axis, and in-line in the y-axis), and output factors. Based on this report, energies of 10 MV or above are not appropriate for small fields due to increasing neutron contamination and secondary electron range (34). ion chambers,

TLD dosimetry systems, radiographic films, gafchromic films, MOSFET (The metal–oxide–semiconductor field-effect transistor), gel dosimeter systems, diode, and diamond detectors are examples of dosimeter equipment. Each detector reacts differently to ionizing radiation, and each has pros and cons (17).

2.5.3. Physics of small field dosimetry

Compared to conventional radiotherapy, the problems encountered in small field dosimetry are mostly due to the electron transport resulting from photon interaction. In general, small field problems can be grouped under two subheadings; beam-related issues and detector-related issues (7).

2.5.3.1. Beam-related issues

Ionizing radiation interacts with an absorbing medium in two ways. The kinetic energy of the incoming photons is transmitted to the electrons in the surrounding medium. This is called indirect interaction. Secondary interactions performed by these electrons in the energy-transferred medium are called direct interactions (11). Lateral charged particle balance, also known as electronic balance, is the condition in which the quantity (total energy) of secondary electrons entering and exiting the same volume is equal. It is a state of equilibrium (31). Absorbed dose measurements in conventional field dosimetry are done in ion chambers with wall thicknesses that meets the requirement that the absorbed dose and collision Kerma are identical (11, 31). The small field dosimetry, on the other hand, is not without flaws. Two of these problems are related to the incoming beam, and one is due to the characteristics of the detector used for measurements. If at least one of these 3 problems occurs, depending on the density of the material being measured (e.g. water) and the energy of the incident photon (e.g. 6 MV), the area of interest is stated as a small field (e.g. < 3 x 3 cm^2) (31).

<u>Absence of electronic equilibrium:</u> Arises when the range of the secondary electron is greater than the beam boundary in the central beam axis; in other words, the maximum lateral range of the secondary electron is smaller than the FWHM of the photon beam and as a result, the electronic equilibrium is lost.

The dose and collision Kerma (K_{col}) absorbed in the medium are not equal. Figure 2.21 depicts the photon beam area diameters where equilibrium is attained and lost for various energies. $D/K_{col}=1$ is the field diameters at equilibrium. $D/K_{col} < 1$ represents the area diameters where the lateral balance is lost.

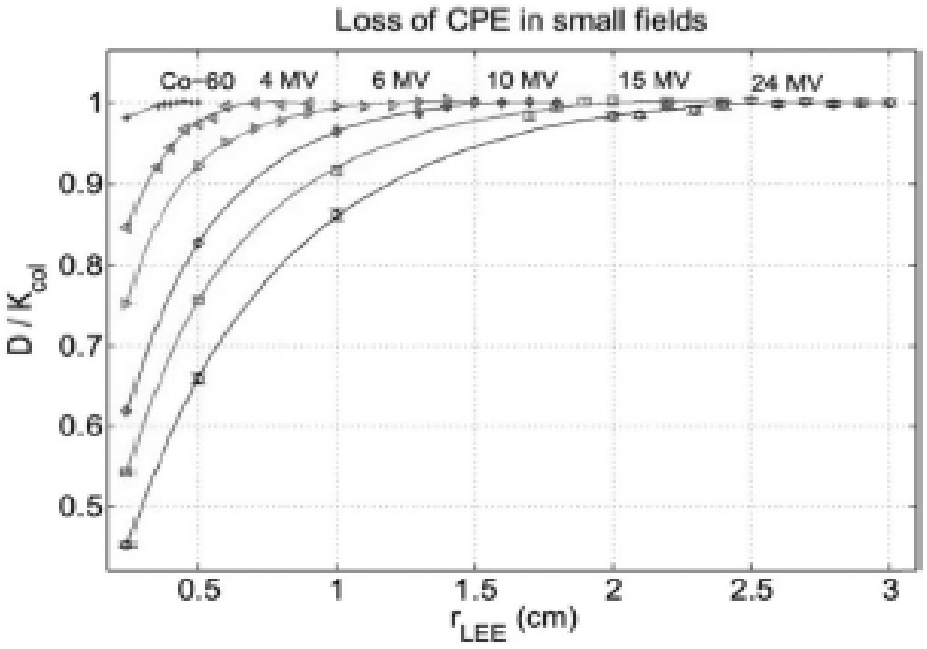

Figure 2.21 The photon beam area diameters where equilibrium is attained and lost for various energies (4)

Partial occlusion of primary photon beam source: In linac devices, the main source size is typically 5 mm or smaller. When the field size is significantly lower than the main source size, a portion of the incoming photon beam will be blocked by the collimators resulting in the overlapping of the penumbra as shown in Figure 2.22. The left image depicts the large beam condition, whereas the right image depicts the small field condition, with penumbra overlapping since the field size was less than the source size determined and called as partial occlusion of the source. This is a significant effect in small field dosimetry; as the beam spectrum changes in direct proportion to the decrease in field size, as does the beam output.

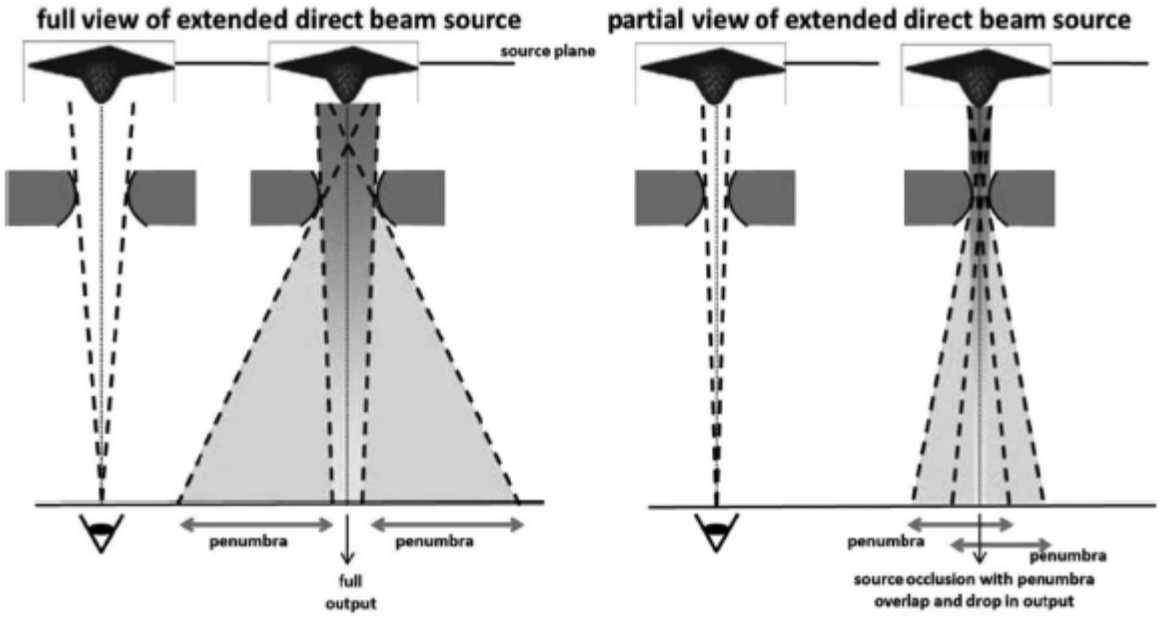

Figure 2.22 Blocking of the main source by collimator at small fields (4)

2.5.3.2 Detector-related Issues

The third issue encountered in small field dosimetry is the presence of detectors used for measurements. It has two effects on beam quality: the perturbation effect and volume averaging. (6, 31).

Even though the measurements are conducted in water, the cavity of the ion chambers used in the absorption dose measurements, is a medium with a different density than water. Charged particle interactions between the medium and water create perturbation effects. In conventional field dosimetry, the results read in high-energy photon beam calibrations produced with ion chambers are adjusted by using stopping power and perturbation correction factors when computing absorbed doses. This is known as the Bragg-Gray cavity theory (11).

Since electronic equilibrium is lost and substantial dose gradients arise in small-field dosimetry compared to large-field dosimetry, the Bragg-Gray cavity hypothesis is no longer viable. The detector's presence causes distortion effects. Monte Carlo simulations have

shown that the perturbation effect in measurements made with ion chambers in small fields has three components; wall material, electrode material, and detector material. Of these 3 perturbation effects, it was observed that the perturbation effects caused by the wall and electrode material were so small that they could be ignored. The volume average effect, which arises depending on the material of the detector employed, is the greatest perturbation effect in the small field dosimetry. Due to the signal generated by a detector is changing with the dose absorbed in the detector's sensitive volume and therefore its homogeneity, the density difference and volume effect are the determinants of the correction factors to be used. (6, 31).

Also, since the perturbation effect and the volume average impact the calculations of the absorbed dose measurements in the small field dosimeter, the length of the detectors cavity should be in lengths where electronic balance can be achieved. Figure 2.23 (35) shows the volume averaging effect depending on the ion chamber length used in small field dosimeter measurements for the calibration of 6, 7, and 10 MV FFF photon beams for different device models (4).

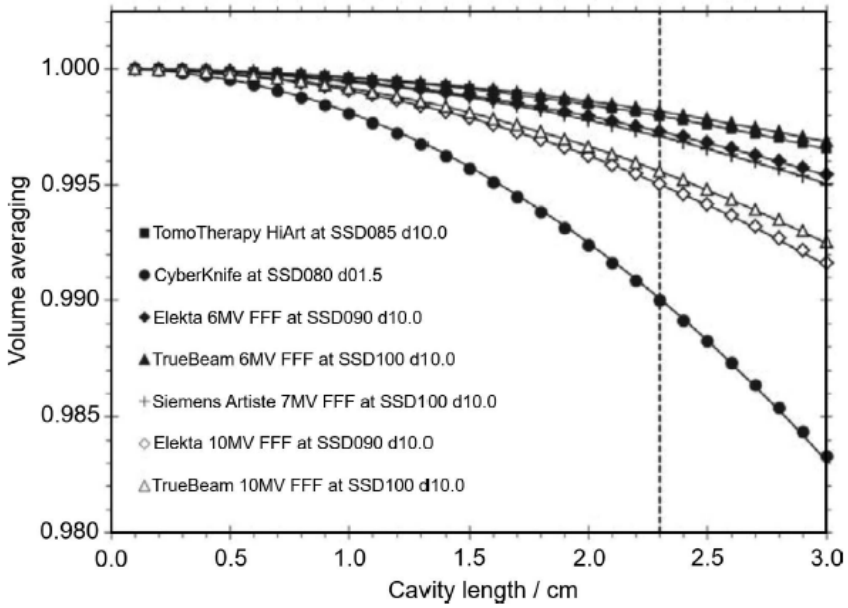

Figure 2.23 The volume averaging effect induced by the ion chamber length/cm used for small field dosimetry (35)

2.5.3.3 Effect of geometric field size and radiation field size

In linac-based devices, field size, which is a plane perpendicular to the central axis, is set using MLCs and jaws and is represented in FWHM, the width equal to the 50% dose value of the lateral profiles. It is defined by two components, the geometric field dimension, and the irradiation field dimension. For the large field sizes, the geometric field size and the irradiation field size are equal to each other. In small fields, due to partial blocking of the source by the collimators and the absence of electronic equilibrium, the geometric field size adjusted by the collimators is smaller than the irradiated field size expressed as %50 of the isodose line. In this case, since there's no correlation between the geometric field size and irradiation field size, the penumbra at the edges of the area overlaps with the area, as shown in Figure 2.24. This effect is expressed as widening of area. Because the detector response and perturbation factors in the small field dosimeter are directly related to the irradiation field sizes, jaw and collimator calibrations affect the direct output measurements, and thus the MU values calculated by the dose calculation algorithms in the TPS cause the dose to be calculated as an overdose (6, 31). Sharpe et al. showed that the effect of a 2 mm deviation in the field size on the output measurements was 16%, and the effect of a 1 mm deviation on the output measurements was 8% in the 1 x 1 cm^2 small field dosimeter measurements (36).

2.5.3.4. Reference dosimetry (Alfonso formalism)

Photon dosimetry measurements for 10 x 10 cm^2 reference fields are conducted in conventional radiotherapy utilizing ion chambers. Reference dosimetry calculations have been revised by Alfonso et al for small fields where electronic equilibrium is lost and problems such as volume averaging and perturbation effects occur due to detector material and density, and detector-specific correction factors are defined by introducing machine

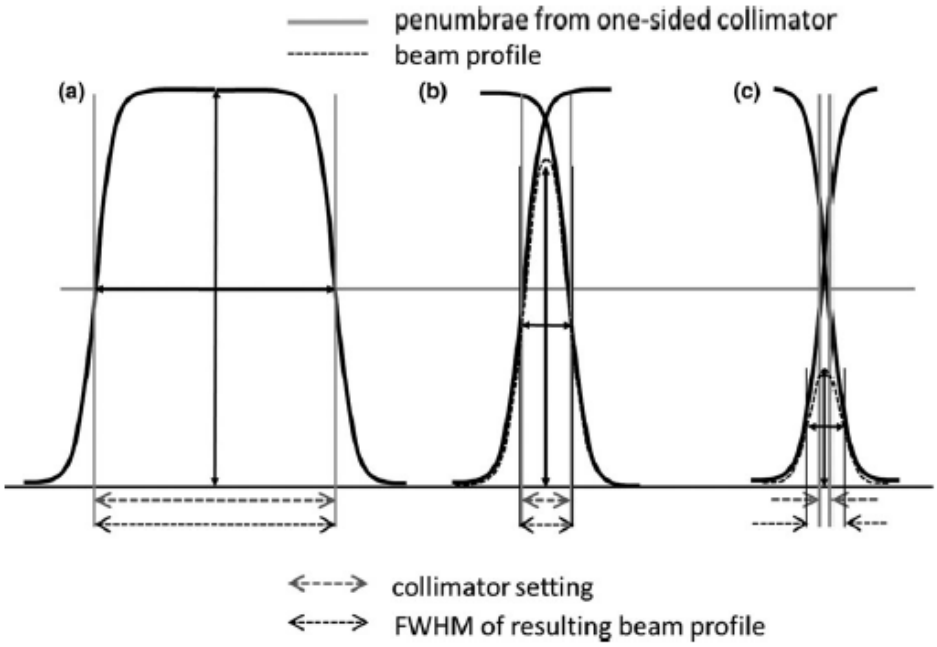

Figure 2.24 (a) Geometric field size is equal to irradiation field size (FWHM)
(b) Geometric field size < irradiation field size
(c) Geometric field size << irradiation field size
(Widening of area, overlapping of penumbra) (4)

specific reference field definition for cases where a reference field sizes of 10 x 10 cm^2 could not be obtained as shown in the given Formula 1 (6, 4, 31, 37).

$$k_{Q_{clin},\, f_{msr}}^{f_{clin},\, f_{msr}} = \frac{D_{w,\ Q_{clin}}^{f_{clin}} / D_{w,\ Q_{msr}}^{f_{msr}}}{M_{Q_{clin}}^{f_{clin}} / M_{Q_{msr}}^{f_{msr}}} \qquad (1)$$

There are two methods for determining detector-specific correction factors. The first approach, commonly known as the gold standard, is Monte Carlo simulations. Modeling the linac device and detectors used in this technique yields the correction factors. The second technique is the experimental method, in which a tissue-equivalent detector with high resolution known to have a correction factor near to 1, such as gafchromic film, TLD, plastic

scintillator, is picked as a reference detector and the field output factor is computed is used. Specific correction factors for various detectors are calculated using this computed field output factor as shown at the given Formula 2 (31).

$$\Omega_{Q_{clin},\,Q_{msr}}^{f_{clin},\,f_{msr}} = \frac{M_{Q_{clin}}^{f_{clin}}}{M_{Q_{msr}}^{f_{msr}}} . k_{Q_{clin},\,Q_{msr}}^{f_{clin},\,f_{msr}} \qquad (2)$$

2.5.3.5. Relative dosimetry

The Daisy-Chain technique, which has been described in the literature, is used to determine relative output factors. This technique employs three distinct field sizes; the reference field (10 x 10 cm^2), a specified intermediate region of 3 x 3 or 4 x 4 cm^2, and the clinical field size. For the clinical field size for which the output factor will be calculated, the ionization amount measured with the relative detector is normalized to the measurements made with the ion chamber in the reference area of 10 x 10 cm^2, taking into account the ionization amount obtained with the measurements made with both the ion chamber and the relative detector for the specified intermediate field size (3 cm x 3 cm or 4 cm x 4 cm) as shown at the given Formula 3 (31).

$$OF_{detector} = \frac{M_{FS,detector}}{M_{3x3,detector}} . \frac{M_{3x3,IC}}{M_{10x10,IC}} \qquad (3)$$

Relative output factor measurements produce different findings depending on shaping the region by a jaw/MLC or cone, and it is a factor determining TPS dose calculations. Another critical element influencing output factors and hence TPS beam modeling in small field measurements is the detectors used for relative dosimeter measurements. The size (inner radius/length), wall, and electrode material of the detector to be used should be chosen in line with the relative dosimeter readings to provide a homogenous signal throughout the detectors sensitive volume and decrease the influence of the volume average (31). Again, the output factor measurements are affected by whether the detectors are parallel or perpendicular to the center axis during the measurements (8).

2.5.3.6. Detectors used for reference and relative dosimetry in linac-based small field measurements

Manufacturers have created a variety of detectors with varying physical characteristics appropriate for reference and relative dosimetry (7). When the area of interest is small field sizes, the best suitable detectors should have minimal energy dependence to produce a high signal to noise ratio with a noise reduction. Furthermore, it should be made from a substance with an atomic number equal to or close to that of water, implying that it is water equivalent (density=1 g/cm^3) to obtain high resolution and high sensitivity. These characteristics are not fully provided by any detector utilized in small field dosimeters. Detectors, on the other hand, maybe classified into five categories based on how well they satisfy these criteria (38,39).

1) Calorimeters: Graphite, water
2) Solid-state: MOSFET, diode, TLD, diamond
3) Liquid detectors: Liquid ionization chambers,
4) Chemical detectors: Gafchromic film, gel dosimeter
5) Plastic scintillators

In this dissertation, gafchromic film was used for the reference dosimetry measurement, whereas ion chambers, diode, and diamond detectors were used for the relative dosimetry measurements; hence, only the features of these detectors are explained in this section.

1) Gafchromic film: It is made up of a 28 micrometers thick active layer, which consists of monomers compounds transforming to polymers under radiation, around sandwiched between passive layers about 125 micrometers thick. Gafchromic films are one of the most used techniques for measuring reference dosimetry because they have no energy dependence, are made from tissue-equivalent materials, need few correction factors, and have excellent spatial resolution and sensitivity. Aside from its benefits, there are several factors to consider when calculating the dose absorbed in water using gafchromic film. Post-irradiated images should be scanned using high

optic density scanners, and images converted to optic density should then be translated to absorbed dose values using appropriate analytic tools such as Matlab or ImageJ. The most significant drawback of gafchromic films is that they are influenced by ultraviolet (UV) light. Again, challenges such as scanner heating between various scanner types may have an impact on the dose-response of gafchromic films. (17, 40, 41).

2) Ion chambers: As illustrated in Figure 2.25, cavity ion chambers (thimble or cylindrical) with a sensitive volume of 0.3-0.6 cc are detectors built of tissue-equivalent material that is widely employed in conventional radiotherapy (6). Their sensitivity is lower when compared to semiconductor detectors. Since the presence of ion chambers causes perturbation effect and volume average in small field, in relative dosimeter measurements, the sensitive volume of the ion chambers to be used must provide conditions in which the lateral electronic balance is not lost for the size of the area to be measured. Due to their underestimated response, ion chambers used in traditional radiotherapy are unsuitable for small field dosimetry. Mini and micro-ion chambers (between 0.001 cc and 0.002 cc) with very small sensitive volumes are commercially available from various manufacturers, and are appropriate for small field dosimetry experiments (31, 42). Bozidar Casar et al. examined the impact of positioning the ion chamber parallel or perpendicular to the central axis during the measurement on the output correction factors using 7 different ion chambers with varying sizes of sensitive volumes from different manufacturers. Although it is common practice in clinics to position the ion chambers perpendicular to the central axis, this study revealed the benefit of parallel positioning (4).

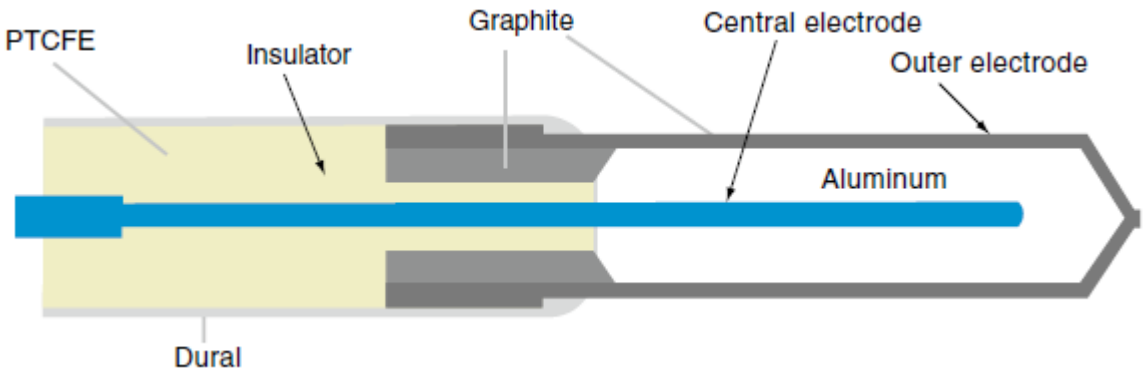

Figure 2.25 Air-filled cavity chamber design (16)

3) Diode detectors: Silicon diodes, which are employed in small field relative dosimeter measurements, are semiconductor detectors that come in two variations: n-type and p-type. The most significant benefit of silicon diode detectors over ion chambers is that they may be manufactured with a very tiny sensitive volume (0.002 cc) and high sensitivity (high spatial resolution). When the silicon crystal is doped with phosphorus, a group V element in the periodic table with 5 valence electrons in the outermost orbit, a bond is formed between the silicon atom and the phosphorus's 4 electrons. The phosphorus 5th electron is still free in the crystal. These detectors are referred to as n-type. The p-type refers to silicon diodes that have been doped with boron, which is found in the periodic table's group III, and has three valence electrons in the outermost orbit. A positive gap is formed when three electrons bind together. When the silicon crystal is subjected to ionizing radiation, a current forms between the electron-hole pairs depending on the energy and dose rate, and the electrometer reads this signal. Diode detectors have both advantages and drawbacks. Due to the angle dependence, they should be positioned parallel to the central axis in measurements. They have energy dependencies. Even if they are not affected by open-air pressure, they are impacted by temperature as in ion chambers, and correction factors must be applied. N-type detectors can be damaged at high dose rates, and therefore, p-type is more commonly used than n-type in relative dosimetry in clinics. Again, diode detectors has two different types, shielded and unshielded.

When a tungsten-like substance is employed as a build-up cap in shielded diode detectors, a linear dose-response cannot be generated owing to the contamination of low-energy scattered electrons in the measurements (11, 31, 42, 43).

4) Diamond detectors: Diamond detectors offer benefits over ion chambers and diode detectors in that they do not rely on energy in relative dosimeters and can be manufactured in extremely small sizes. Clinical radiotherapy employs synthetic diamond detectors. When compared to ion chambers, they are made of tissue-equivalent materials and need relatively small correction factors due to very minimal perturbation effects (31, 42).

2.5.3.7. Impact of small field dosimetry over beam modelling in treatment planning systems

To accurately calculate tumor and OAR 3D dose distribution during SRS/SRT/SBRT treatments by the existing dose calculation algorithms in TPS, the deep dose, profile, and output factor values obtained as a result of the absorbed dose measurements performed in the water phantom using reference and relative detectors, which is the dosimetric data of the beam, are used in the modelling of TPS. Beam models, in other words, are the data sets used by TPS algorithms to forecast 3D dose distributions for the given look-alike measurement geometries. When opposed to conventional treatments, small field treatments deliver higher dose rates in 1-5 fractions. Overdose of healthy tissue indicate that the biological damage is so severe that the tissue is unable to restore itself. As a result, to compute properly, the treatment dose applied by the dose calculation algorithms used in TPS's must be accurately modeled. Particularly due to the volume averaging effect caused by the detector used in measurements in small fields or the partial blocking of the source caused by the finite size of the primary source by the collimators, the measured dosimetric parameters, and therefore beam modeling are affected and TPS's result in incorrect dose calculations. The PDD and profile measurements made by Woong Cho et al with 3 different detectors (CC01 and CC13 ion chambers and Edge n-type silicon detector) with different sensitive volumes, revealed

that even though the tumor dose distribution was not affected much in beam modeling in SBRT applications, OAR doses were found to be % 2 percent higher than the prescribed dose, which is significant. Although it varies according to treatment planning systems, Figure 2.26 depicts beam-modelling and treatment planning sample flowchart (31, 44, 45).

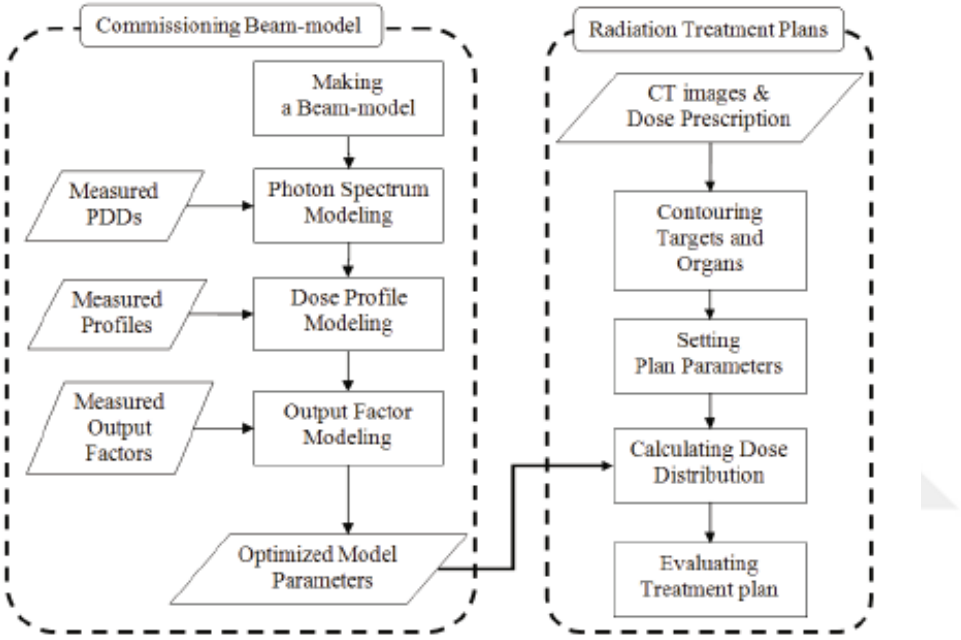

Figure 2.26 Sample flow-chart to be followed for beam-modeling and treatment planning (44)

2.5.3.8. Brief description of TPS dose calculation algorithms

The existing dose calculation algorithms in TPS are divided into factor-based and model-based algorithms. Although factor-based algorithms are still used in devices dedicated to stereotactic applications, the algorithms commonly used in clinics are model-based algorithms. Model-based algorithms are divided into 4; pencil kernel, point kernel (collapsed cone or convolution/ superposition methods), grid-based Boltzmann solutions, and Monte

Carlo applications. These algorithms make dose calculations based on primary photon source and secondary charged particle interactions (46, 47, 48).

Dose distributions are computed by taking into account all the interactions caused by scatterings, such as the homogeneous or heterogeneous nature of the tissue, collimator characteristics, beam shape (flat or unflat), and patient geometry. The most significant distinction between the algorithms is in terms of accuracy and speed. The pencil kernel and the point kernel are two distinct kernel-based dose algorithms. The primary photon and secondary electrons are represented in these methods, the photon's energy distribution is described as a "kernel," and the absorbed dose is modelled throughout the entire volume. In contrast, in Monte Carlo techniques, the program simulates all potential interactions one by one, and the absorbed dose is computed for each particle in the volume of interest until it exits the volume. Because each interaction is simulated one at a time and the absorbed dose is determined as a consequence of a random number of possibilities, all system parameters such as material, density, thickness, and so on should be represented properly. For example, all components of the linac head, such as the primary source, target, flattening filter, jaws, MLC must be represented, and therefore Monte Carlo simulations take a long time (46, 47, 48).

In terms of accuracy, the pencil beam method cannot provide precise dose measurements when compared to Monte Carlo, especially in heterogeneous tissues (such as lungs or paranasal sinuses, which are air-filled organs). Monte Carlo, on the other hand, is significantly slower since it simulates the interactions and energy transfers of main and secondary charged particles inside the tissue using a random number of probability computations (46, 47, 48).

3. MATERIALS AND METHODS

3.1 Overview of equipment

All measurements in this dissertation were taken in Istanbul Oncology Hospital using an Elekta brand Versa HD Agility 160 MLC linear accelerator device. Seven different active detectors with sensitive volumes appropriate for small field dosimeters from various manufacturers were used in our study. Ion chambers with a sensitive volume fewer than 0.01 cm^3 are called micro ion chambers, while those with a sensitive volume between 0.01 cm^3 and 0.03 cm^3 are called mini ion chambers. In our study, we used two mini ion chambers (IBA CC04 and PTW 31022 Pinpoint 3D), two micro ion chambers (Standard Imaging Extradin A16 and IBA CC01), one synthetic diamond detector (PTW 60019 micro Diamond), one n-type shielded diode detector (Sun Nuclear Edge), and one p-type unshielded diode detector (PTW 60018 SRS diode). Table 3.1 summarizes the properties of the detectors.

Table 3.1 Characteristics of the detectors used for measurements

								
Manufacturer	IBA	IBA	IBA	Standard Imaging	PTW Pinpoint 3D	PTW microdiamond	PTW SRS Diode	Sun Nuclear
Model	CC13	CC01	CC04	Extradin A16	31022	60019	60018 (p type) (Unshielded)	Edge (n type) (Shielded)
Sensitive Volume	0.13cm^3	0.01cm^3	0.04 cm^3	0.007 cm^3	0.016 cm^3	0.004 mm^3	0.03 mm^3	0.019mm^3
Central Electrode	C552	Steel	C552	C552	Al	Synthetic Diamond (Carbon)	Silicon	Silicon
Reference Depth	1.8 mm	0.6 mm	1.2 mm	0.72 mm	2.4 mm from chamber tip	1 mm from detector tip	0.74 mm from detector tip	0.3 mm
Orientation	Perpendicular	Perpendicular	Perpendicular	Perpendicular	Perpendicular	Parallel	Parallel	Perpendicular
Nominal Voltage	±300 V	±300 V	±300 V	±300 V	±300 V	±0 V	±0 V	±0 V

The IBA Smart Scan water phantom (Figure 3.1) was used for the measurements taken with active detectors.

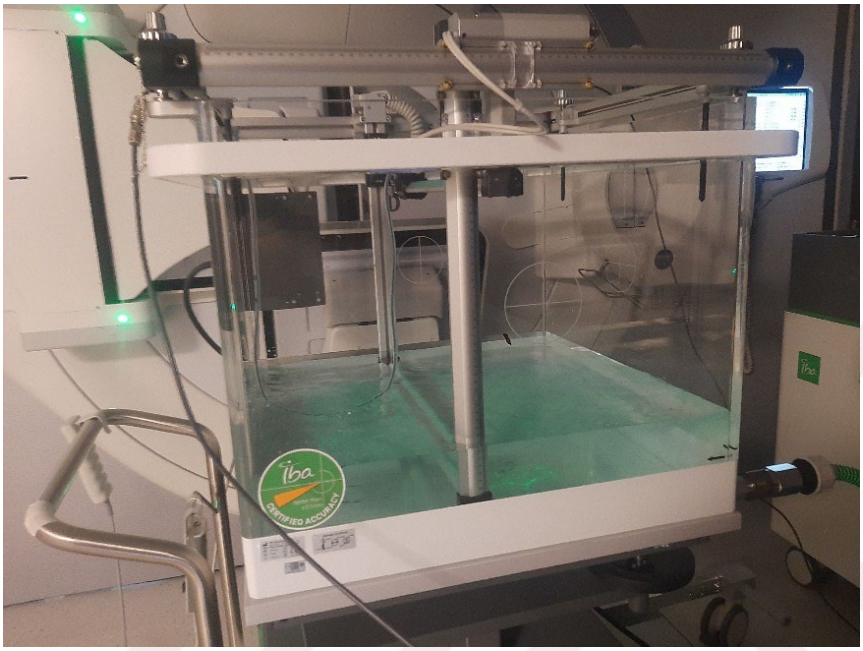

Figure 3.1 IBA Smart Scan water phantom

In our study, gafchromic film (Figure 3.2) was used as the passive detector. The RW3 solid phantom was used to measure gafchromic films.

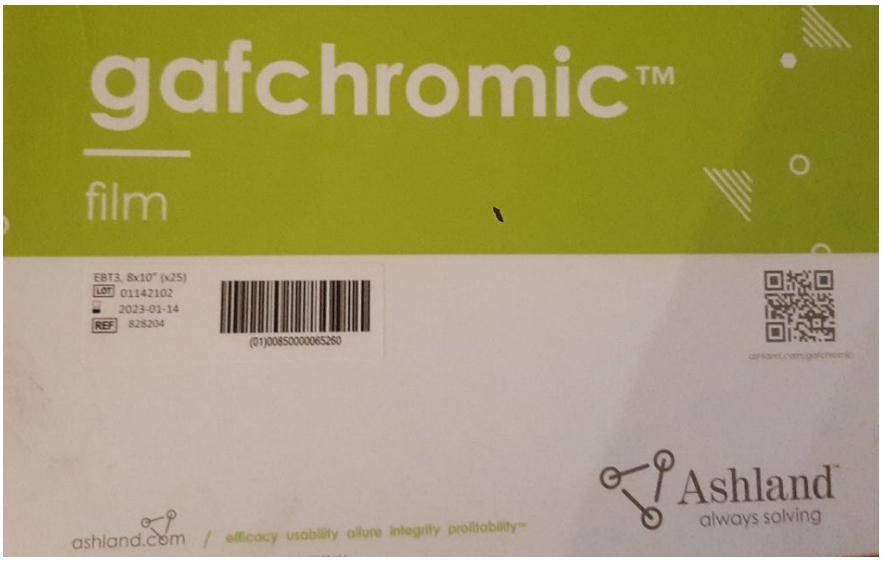

Figure 3.2 Ashland EBT 3 gafchromic film (LOT 01142102)

The equipment (software and hardware) used in our study is summarized below.

1) Elekta Versa HD Agility 160 MLC linear accelerator
2) Active detectors: IBA CC13, IBA CC04, IBA CC01, SI Extradin A16, PTW 31022 Pinpoint 3D, Sun Nuclear Edge diode (shielded), PTW 60019 micro Diamond, PTW 60018 diode SRS p (unshielded)
3) Passive detector: Ashland EBT3 gafchromic film
4) IBA Smart Scan water phantom
5) IBA Scanditronix Wellhöfer Dose1 electrometer
6) RW3 solid phantom
7) EPSON Expression 10000 XL scanner (48-bit RGB, 150 dpi resolution, transmission mode)
8) Fiji image processing software
9) T-test statistical analysis tool

To reduce the volume average effect seen in small field dosimetry, all calculations in this dissertation were made using the Daisy Chain technique proposed in the TRS-483 protocol (Formula 3). The Daisy Chain technique was performed in an ion chamber with a sensitive volume of 0.13 cc.

3.2 Intermediate field size calculation with Daisy Chain technique for IBA CC13

Formula 4 is used to calculate the field size where lateral electronic balance is established for the IBA CC13 ion chamber with a sensitive volume of 0.13 cc to be utilized for the Daisy Chain technique (4).

$$FWHM \geq 2r_{LCPE} + d \qquad (4)$$

The following CC13 characteristics were extracted from the manufacturer's documentation (49):

5.8 mm length of the cavity

3.0 mm radius of the cavity

0.4 mm wall thickness

the detector length in the longitudinal direction;

$d_l = l + t_{wall} = 5.8 + 0.4 = 6.2$ mm

radial direction;

$d_r = 2 (r + t_{wall}) = 2 (3.0 + 0.4) = 6.8$ mm

means $d_r > d_l$.

based on Formula 5 (4);

$$r_{LCPE} = 8.396 \times TPR_{20,10}(10) - 4.382 \quad (5)$$

Energy	**$TPR_{20,10}$ (10)**	**r_{LCPE} (mm)**	**FWHM**
6 WFF	0.674	12.77	3.234
6 FFF	0.675	12.85	3.250

For establishing lateral electronic balance, the intermediate field size should be selected equal to or greater than 3.234 mm and 3.250 mm for 6 WFF and 6 FFF photon beams, respectively, based on Formula 4.

3.3 Detector position in water phantom measurements

The stem effect that will occur in water phantom measurements affects the output factor and profile measurements. TRS-483 (4) protocol was followed to minimize the stem

effect. Measurements were taken by positioning IBA CC13, IBA CC04, IBA CC01, SI Extradin A16, PTW 31022 Pinpoint 3D, Sun Nuclear Edge diode detector perpendicular to the beam direction, and PTW 60019 micro Diamond, PTW 60018 diode SRS detector parallel to the beam direction.

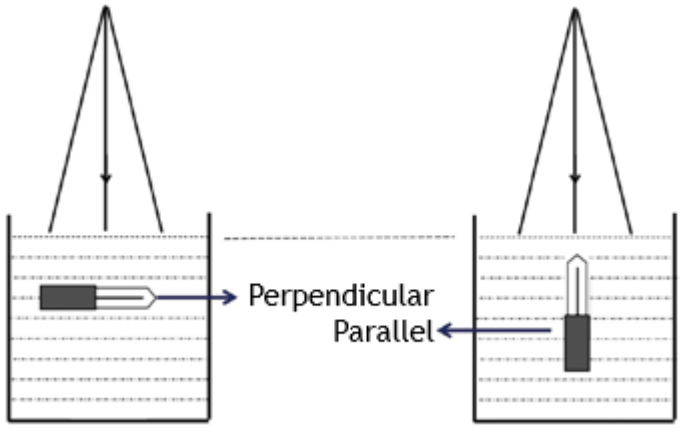

Figure 3.3 Detector orientation inside the water phantom

3.4 Measurements with IBA Smart Scan water phantom

The steps specified in the following items were carried out separately for 7 active detectors. Measurements were taken by positioning each detector in the water phantom at the EPOM as specified in the manufacturer's catalogs. The EPOM for the ion chambers was calculated as 0.6 radii.

1) CAX deviation was done with IBA myQA software for the field size of 10 x 10 cm^2 at SSD: 100 cm and depth:10 cm to validate that being in the center of the irradiation field, and it was verified whether there was any deviation from the central axis and necessary shifts were made if any.
2) The inline and crossline profiles were evaluated with IBA myQA software for the field sizes of 0.8 x 0.8 cm^2 at SSD: 100 cm and depth :10 cm following CAX

deviation, and it was checked whether there was any deviation from the central axis and if required changes were made.

3) Finally, for a field size of 0.8 x 0.8 cm^2, the dose was measured with the IBA myQA software at the center, + 0.2 mm, and - 0.2 mm in the inline direction, and the point at which the signal was maximum was determined.

3.5 Output factor measurements for 7 active detector

Each field size of 0.5, 0.8, 1, 2, 2.5, 3, 3.5, 4, and 5 cm^2 at SSD was measured three times. The measurements were taken and recorded using an IBA Scanditronix Wellhöfer Dose1 electrometer for the point where the maximum signal is obtained. Since polarization correction was applied for the ion chambers in our calculations, the ion chamber measurements were taken separately at +/- 300 Volts. The bias voltage for solid-state detectors is set to 0 volts, as described in the manufacturer's catalogs.

3.6 EBT 3 gafchromic film measurements with RW3 solid phantom

The protocol specified in the literature was followed for the calibration and dosimetry of EBT3 radiochromic films (8, 50). Films to be calibrated and irradiated were selected from the same lot.

1) Calibration films were cut into 14 equal pieces using a gladiator following the protocol of Bozidar Casar et al (8, 50). Due to the directional dependencies of the EBT3 films, the films were cut into equal strips so that the long edge of the film was parallel to the long edge of the Epson Expression 10000 XL scanner, and the upper right corners were marked by specifying the dose rates to be irradiated. The calibration films were individually irradiated in 50 MU increments from 50 MU to 600 MU at SSD: 100 cm and depth: d_{max} placed in the center of the solid phantom, respectively. 500 MU was irradiated twice with 6 MV WFF. Two non-irradiated (0 MU) calibration films are left.

2) After the calibration films, the dose films were cut, each area size was written in the upper right corner, taking into account the direction of the films, and then irradiated. Again, the protocol of Bozidar Casar et al (8,50) was followed. Area size of 0.5, 0.8, 1, 2, 2.5, 3, 3.5,4, 5, and 10 cm^2 was irradiated 3 times with 500 MU to reduce uncertainties that may occur during the scanning process. The films were individually irradiated at SSD: 90 cm and depth: 10 cm by placing them in the center of the solid phantom (Figure 3.4).

Figure 3.4 Irradiation of gafchromic films

Since gafchromic films are affected by UV light and are directional dependent, a very strict protocol has been followed in the processes. The films were not touched with bare hands and gloves were worn. Film cutting and irradiation were done in a dark environment.

3.7 Scanning procedure of EBT 3 gafchromic films (51, 52)

Gafchromic films consist of monomer compounds that turn into polymers under radiation (17,40,41). It is advised in the literature to wait at least 24 hours for the polymerization to be finished and stabilized before reading the optical density measurements. For this purpose, after the completion of irradiations, 36 hours past before scanning of the 6 WFF calibration and dose films. Scans were performed in a dark environment with the Epson Expression 10.000 XL scanner. The scanner software for Windows 11 was installed to the computer and the automatic photo correction settings were turned off by selecting

Professional Mode. The driver is set to 48-bit color, positive film, and 150 dpi resolution. Since the reading was made in the transmission mode, the films were fixed with a 3.8 mm thick 30 x 40 cm plexiglass sheet. The scanner was warmed up 30 minutes before the scans. By making 5 previews before scanning, the lamp of the scanner was warmed up. To minimize the uncertainties that may occur during scanning, 3 films of each field were scanned 5 times and the films were saved as .tiff (Figure 3.5).

Figure 3.5 Scanning process of gafchromic films

3.8 ImageJ analysis software for the conversion of optical density values to absorbed dose at EBT3 gafchromic film (51)

3.8.1 Calibration curve

Calibration films irradiated with 6 WFF and saved as tiff were split into color channels using ImageJ software and read over a single channel (red channel). The grayscale values for each dose value were read by putting ROIs of width: 150 pixels and height: 150 pixels in the middle of the calibration films and applying backup corrections. Based on the article of Michelle E. Howard et al., the "Rodbard" function were used to construct the dose-response curve (calibration curve) (Figure 3.6) (46). ImageJ software was used to calculate the constants a, b, c, and d in Formula 6. In the calculation, we used dose values as x and grayscale values read by drawing ROI as y.

$$y = d + \frac{(a-d)}{1+\left(\frac{x}{c}\right)^{b}} \qquad (6)$$

a = 47706.03, b = 0.87108, c = 203.209, d = 4841.28

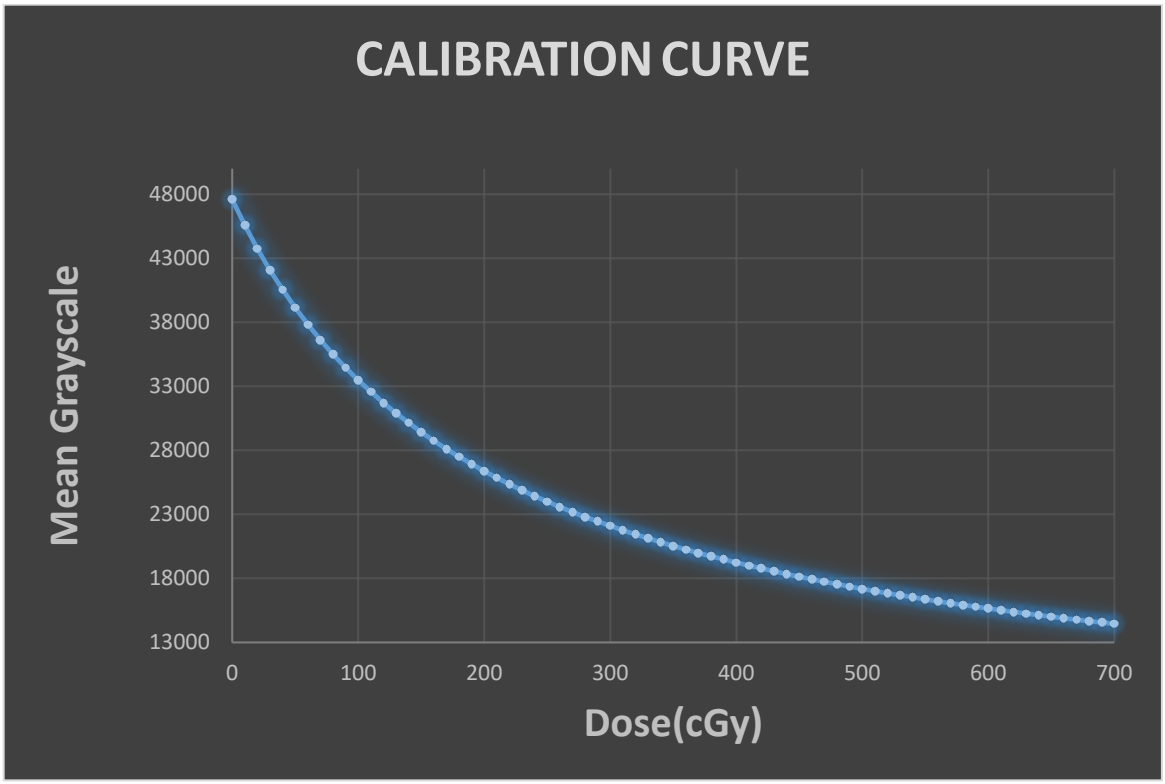

Figure 3.6 6 WFF calibration curve

3.8.2 Dose film readings

3 films scanned 5 times for each field size were split into color channels with Fiji software (a newer version of ImageJ). The readings were taken over the red channel. The grayscale values read from each film scanned five times for three films were averaged. In the film readings, circular ROIs were chosen, and readings were conducted from the dose films centers. After reading the gray scale readings, they were transformed to dose values using Formula 6 and normalized to 500 MU.

4. RESULTS

4.1 6 WFF photon beam

4.1.1 Measurements and calculations

Table 4.1.1.1 3 times measured IBA CC13 ion chamber electrometer readings (cGy) for intermediate field sizes (4 cm x 4 cm) and reference field sizes (10 cm x 10 cm) and corrected values applied polarization correction.

Nominal Field Sizes	IBA $CC13_{+}$(cGy)	IBA CC13_(cGy)	IBA CC13_corrected (cGy)
4.0 cm x 4.0 cm	1.218	1.221	1.220
4.0 cm x 4.0 cm	1.219	1.221	1.220
4.0 cm x 4.0 cm	1.219	1.221	1.220
10.0 cm x 10.0 cm	1.391	1.394	1.393
10.0 cm x 10.0 cm	1.391	1.395	1.393
10.0 cm x 10.0 cm	1.391	1.394	1.393
Mean (4.0 cm x 4.0 cm)	1.220 cGy		
Mean (10.0 cm x 10.0 cm)	1.393 cGy		
Mean (4 cm x 4 cm) / Mean(10 cm x10 cm)	0.876		

Table 4.1.1.2 The mean values of 3 times electrometer readings (cGy) for each detector per field size. Polarization corrections are applied for the ion chambers.

Nominal Field Sizes	IBA CC01	IBA CC04	Extradin A16	PTW Pinpoint 3D (31022)	PTW micro Diamond (60019)	Sun Nuclear Edge	PTW SRS Diode (60018)
0.5 cm x 0.5 cm	0.430	1.221	0.339	0.553	0.273	0.660	0.283
0.8 cm x 0.8 cm	0.663	2.141	0.510	0.828	0.382	0.901	0.397
1.0 cm x 1.0 cm	0.752	2.485	0.587	0.933	0.425	0.985	0.435
2.0 cm x 2.0 cm	0.923	3.172	0.725	1.153	0.501	1.135	0.506
2.5 cm x 2.5 cm	0.952	3.285	0.747	1.183	0.516	1.165	0.520
3.0 cm x 3.0 cm	0.970	3.368	0.767	1.217	0.527	1.190	0.532
3.5 cm x 3.5 cm	0.986	3.427	0.781	1.238	0.536	1.209	0.542
4.0 cm x 4.0 cm	1.006	3.493	0.800	1.263	0.547	1.235	0.554
5.0 cm x 5.0 cm	1.036	3.604	0.824	1.301	0.565	1.274	0.572

Table 4.1.1.3 Mean values of EBT3 gafchromic film readings per field size read 3 times (5 scans each) and normalized to 500 MU.

Nominal Field Sizes	Gafkromik Film (EBT3)
0.5 cm x 0.5 cm	0.345
0.8 cm x 0.8 cm	0.469
1.0 cm x 1.0 cm	0.529
2.0 cm x 2.0 cm	0.639
2.5 cm x 2.5 cm	0.671
3.0 cm x 3.0 cm	0.683
3.5 cm x 3.5 cm	0.705
4.0 cm x 4.0 cm	0.719
5.0 cm x 5.0 cm	0.739
10.0 cm x 10.0 cm	0.819

Table 4.1.1.4 Detector output factors calculated with Daisy Chain technique (OF_{det}) for each field size

Nominal Field Sizes	IBA CC01	IBA CC04	Extradin A16	PTW Pinpoint 3D (31022)	PTW micro Diamond (60019)	Sun Nuclear Edge	PTW SRS Diode (60018)
0.5 cm x 0.5 cm	0.374	0.306	0.371	0.384	0.437	0.468	0.448
0.8 cm x 0.8 cm	0.577	0.537	0.558	0.575	0.611	0.639	0.627
1.0 cm x 1.0 cm	0.654	0.623	0.643	0.647	0.679	0.699	0.688
2.0 cm x 2.0 cm	0.804	0.795	0.794	0.800	0.802	0.805	0.800
2.5 cm x 2.5 cm	0.829	0.824	0.818	0.821	0.825	0.826	0.823
3.0 cm x 3.0 cm	0.845	0.845	0.840	0.844	0.843	0.844	0.842
3.5 cm x 3.5 cm	0.859	0.860	0.855	0.859	0.858	0.858	0.857
4.0 cm x 4.0 cm	0.876	0.876	0.876	0.876	0.876	0.876	0.876
5.0 cm x 5.0 cm	0.902	0.904	0.903	0.902	0.903	0.904	0.905

Table 4.1.1.5 Gafchromic film (EBT3) output factors for each field size(Ω_{EBT3})

Nominal Field Sizes	Ω_{EBT3}
0.5 cm x 0.5 cm	0.421
0.8 cm x 0.8 cm	0.573
1.0 cm x 1.0 cm	0.646
2.0 cm x 2.0 cm	0.780
2.5 cm x 2.5 cm	0.820
3.0 cm x 3.0 cm	0.834
3.5 cm x 3.5 cm	0.861
4.0 cm x 4.0 cm	0.879
5.0 cm x 5.0 cm	0.902

Table 4.1.1.6 Detector specific output correction factors for each field size $k_{Q_{clin},\,Q_{msr}}^{f_{clin},\,f_{msr}}$

Nominal Field Sizes	IBA CC01	IBA CC04	Extradin A16	PTW Pinpoint 3D (31022)	PTW micro Diamond (60019)	Sun Nuclear Edge	PTW SRS Diode (60018)
0.5 cm x 0.5 cm	1.126	1.375	1.135	1.098	0.964	0.900	0.939
0.8 cm x 0.8 cm	0.992	1.067	1.026	0.997	0.937	0.896	0.913
1.0 cm x 1.0 cm	0.987	1.037	1.006	0.999	0.951	0.925	0.939
2.0 cm x 2.0 cm	0.971	0.981	0.982	0.976	0.973	0.969	0.975
2.5 cm x 2.5 cm	0.990	0.996	1.002	0.999	0.994	0.993	0.997
3.0 cm x 3.0 cm	0.987	0.988	0.993	0.988	0.989	0.988	0.990
3.5 cm x 3.5 cm	1.002	1.001	1.007	1.003	1.003	1.003	1.004
4.0 cm x 4.0 cm	1.003	1.003	1.003	1.003	1.003	1.003	1.003
5.0 cm x 5.0 cm	1.000	0.998	0.999	1.000	0.999	0.998	0.997

4.1.2 Graphs

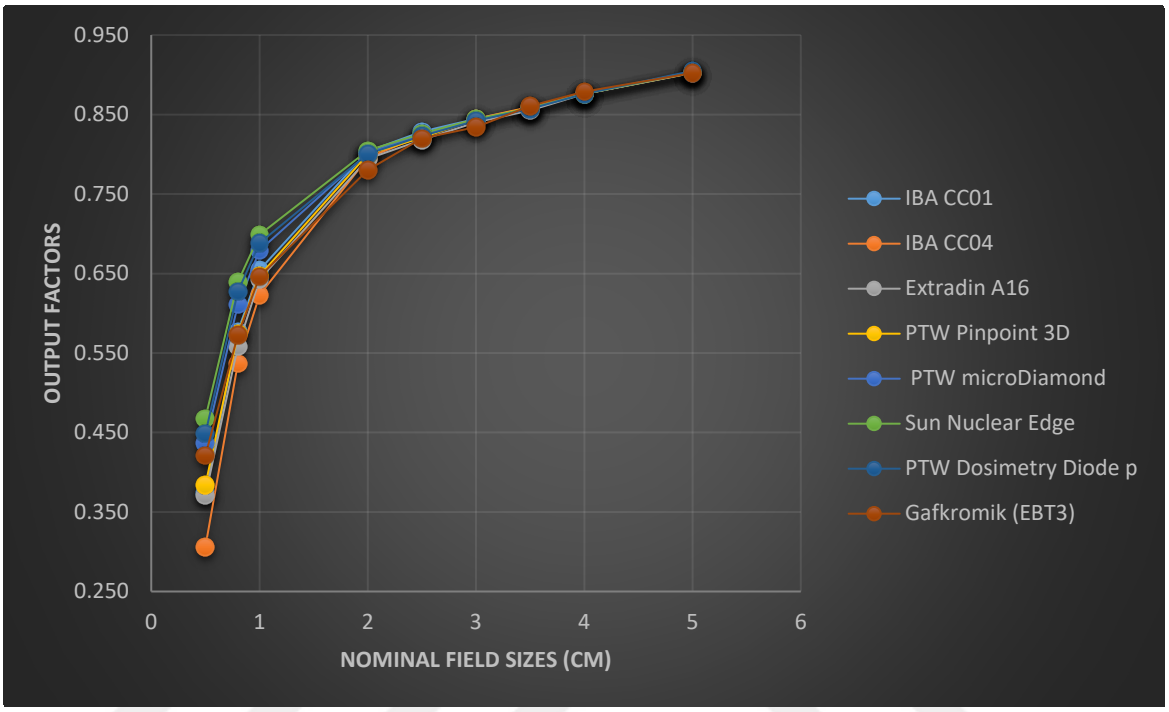

Figure 4.1.2.1 6 WFF photon beam output factor plots against field sizes (OF_{det} and Ω_{EBT3} values)

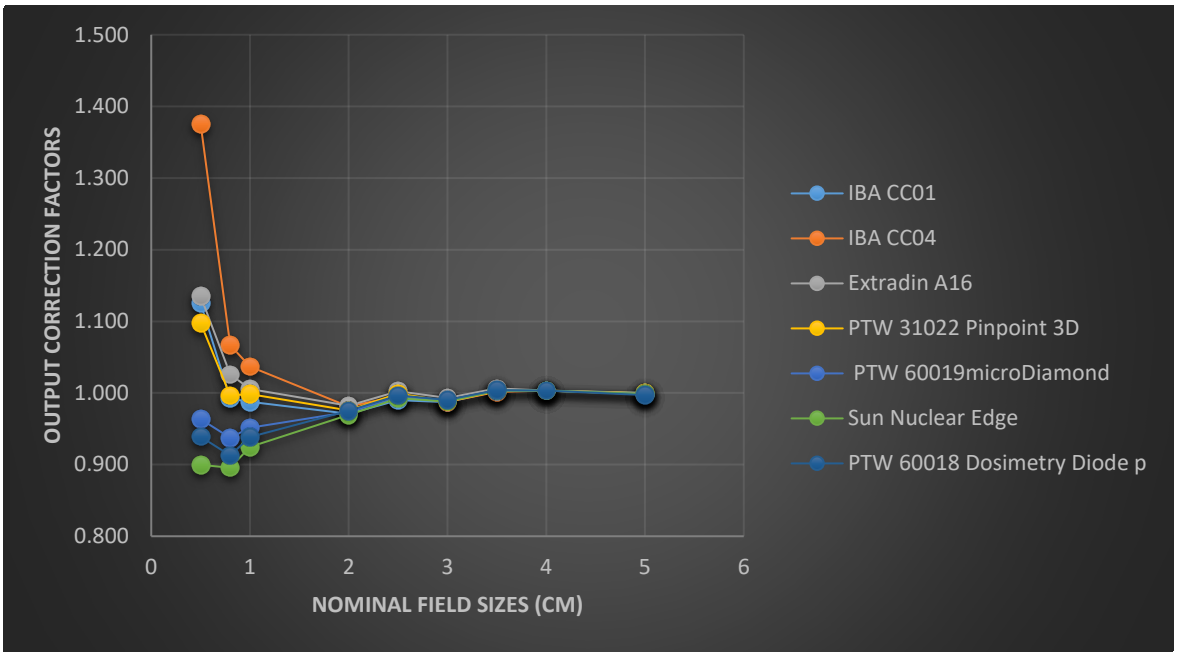

Figure 4.1.2.2 6 WFF photon beam output correction factor plots against field sizes

4.2 6 FFF Photon beam

4.2.1 Measurements and calculations

Table 4.1.2.1 3 times measured IBA CC13 ion chamber electrometer readings (cGy) for intermediate field sizes (4 cm x 4 cm) and reference field sizes (10 cm x 10 cm) and corrected values applied polarization correction.

Nominal Field Sizes	IBA $CC13_{+}$(cGy)	IBA CC13_(cGy)	IBA CC13_corrected (cGy)
4.0 cm x 4.0 cm	1.235	1.237	1.236
4.0 cm x 4.0 cm	1.236	1.239	1.238
4.0 cm x 4.0 cm	1.236	1.238	1.237
10.0 cm x 10.0 cm	1.368	1.372	1.370
10.0 cm x 10.0 cm	1.368	1.373	1.371
10.0 cm x 10.0 cm	1.368	1.373	1.371
Mean (4.0 cm x 4.0 cm)	1.237 cGy		
Mean (10.0 cm x 10.0 cm)	1.370 cGy		
Mean (4 cm x 4 cm) **Mean (10 cm x10 cm)**	0.903 cGy		

Table 4.1.2.2 The mean values of 3 times electrometer readings (cGy) for each detector per field sizes. Polarizatian corrections are applied for the ion chambers.

Nominal Field Sizes	IBA CC01	IBA CC04	Extradin A16	PTW Pinpoint 3D (31022)	PTW micro Diamond (60019)	Sun Nuclear Edge	PTW SRS Diode (60018)
0.5 cm x 0.5 cm	0.414	1.171	0.277	0.493	0.236	0.560	0.260
0.8 cm x 0.8 cm	0.645	2.082	0.491	0.809	0.371	0.881	0.390
1.0 cm x 1.0 cm	0.746	2.494	0.581	0.943	0.425	0.991	0.439
2.0 cm x 2.0 cm	0.930	3.235	0.748	1.180	0.513	1.170	0.522
2.5 cm x 2.5 cm	0.964	3.354	0.776	1.221	0.529	1.204	0.538
3.0 cm x 3.0 cm	0.982	3.431	0.796	1.249	0.540	1.227	0.550
3.5 cm x 3.5 cm	1.001	3.493	0.807	1.270	0.549	1.247	0.559
4.0 cm x 4.0 cm	1.016	3.548	0.824	1.292	0.558	1.267	0.568
5.0 cm x 5.0 cm	1.040	3.640	0.847	1.324	0.572	1.300	0.584

Table 4.1.2.3 Mean values of EBT3 gafchromic film readings per field size read 3 times (5 scans each) and normalized to 500 MU.

Nominal Field Sizes	Gafkromik Film (EBT3)
0.5 cm x 0.5 cm	0.309
0.8 cm x 0.8 cm	0.498
1.0 cm x 1.0 cm	0.549
2.0 cm x 2.0 cm	0.657
2.5 cm x 2.5 cm	0.678
3.0 cm x 3.0 cm	0.688
3.5 cm x 3.5 cm	0.704
4.0 cm x 4.0 cm	0.738
5.0 cm x 5.0 cm	0.763
10.0 cm x 10.0 cm	0.813

Table 4.1.2.4 Detector output factors calculated with Daisy Chain technique (OF_{det}) for each field size

Nominal Field Sizes	IBA CC01	IBA CC04	Extradin A16	PTW Pinpoint 3D (31022)	PTW micro Diamond (60019)	Sun Nuclear Edge	PTW SRS Diode (60018)
0.5 cm x 0.5 cm	0.368	0.298	0.304	0.344	0.381	0.399	0.412
0.8 cm x 0.8 cm	0.573	0.530	0.538	0.565	0.599	0.628	0.619
1.0 cm x 1.0 cm	0.663	0.634	0.636	0.659	0.688	0.706	0.698
2.0 cm x 2.0 cm	0.826	0.823	0.820	0.825	0.829	0.834	0.829
2.5 cm x 2.5 cm	0.857	0.853	0.850	0.853	0.855	0.857	0.854
3.0 cm x 3.0 cm	0.873	0.873	0.872	0.873	0.873	0.874	0.873
3.5 cm x 3.5 cm	0.889	0.888	0.884	0.888	0.888	0.889	0.888
4.0 cm x 4.0 cm	0.903	0.903	0.903	0.903	0.903	0.903	0.903
5.0 cm x 5.0 cm	0.924	0.926	0.927	0.925	0.925	0.926	0.927

Table 4.1.2.5 Gafchromic film (EBT3) output factors for each field size(Ω_{EBT3})

Nominal Field Sizes	**Ω_{EBT3}**
0.5 cm x 0.5 cm	0.380
0.8 cm x 0.8 cm	0.612
1.0 cm x 1.0 cm	0.675
2.0 cm x 2.0 cm	0.807
2.5 cm x 2.5 cm	0.834
3.0 cm x 3.0 cm	0.847
3.5 cm x 3.5 cm	0.866
4.0 cm x 4.0 cm	0.907
5.0 cm x 5.0 cm	0.938

Table 4.1.2.6 Detector specific output correction factors for each field size $k_{Q_{clin},\,Q_{msr}}^{f_{clin},\,f_{msr}}$

Nominal Field Sizes	IBA CC01	IBA CC04	Extradin A16	PTW Pinpoint 3D (31022)	PTW micro Diamond (60019)	Sun Nuclear Edge	PTW SRS Diode (60018)
0.5 cm x 0.5 cm	1.033	1.277	1.252	1.105	0.998	0.953	0.922
0.8 cm x 0.8 cm	1.067	1.156	1.138	1.082	1.022	0.975	0.989
1.0 cm x 1.0 cm	1.018	1.065	1.061	1.025	0.982	0.957	0.968
2.0 cm x 2.0 cm	0.977	0.981	0.985	0.979	0.974	0.968	0.974
2.5 cm x 2.5 cm	0.973	0.977	0.981	0.977	0.975	0.972	0.976
3.0 cm x 3.0 cm	0.970	0.970	0.971	0.970	0.970	0.968	0.970
3.5 cm x 3.5 cm	0.974	0.975	0.980	0.976	0.975	0.975	0.976
4.0 cm x 4.0 cm	1.005	1.005	1.005	1.005	1.005	1.005	1.005
5.0 cm x 5.0 cm	1.015	1.013	1.012	1.014	1.014	1.013	1.012

4.2.2 Graphs

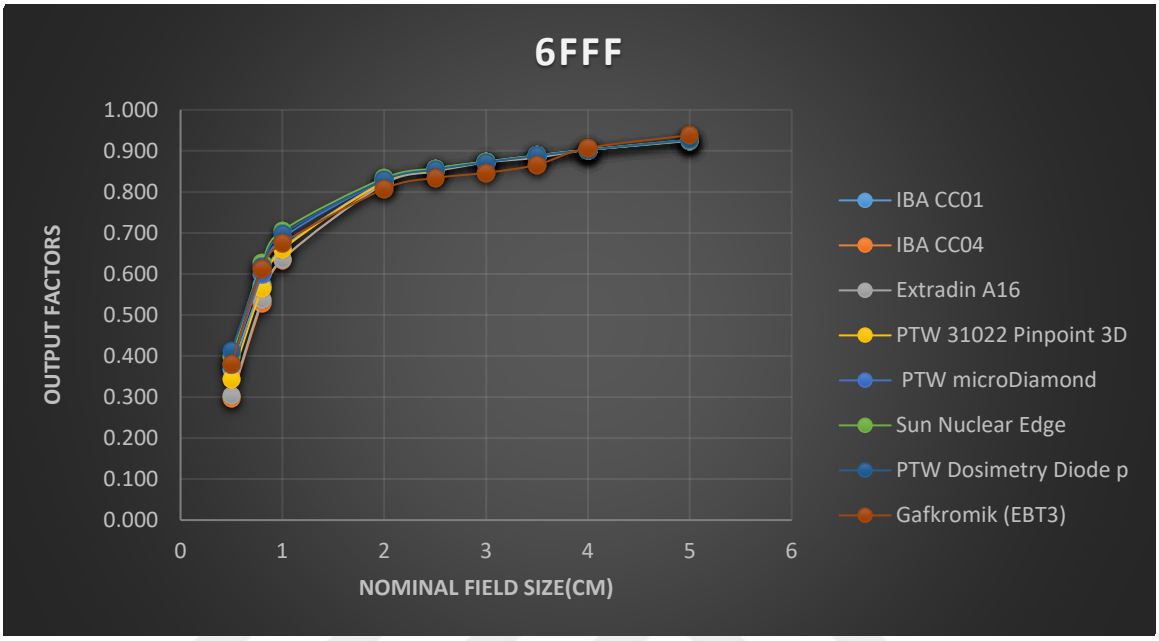

Figure 4.2.2.1 6 FFF photon beam output factor plots against field sizes

(OF_{det} and Ω_{EBT3} values)

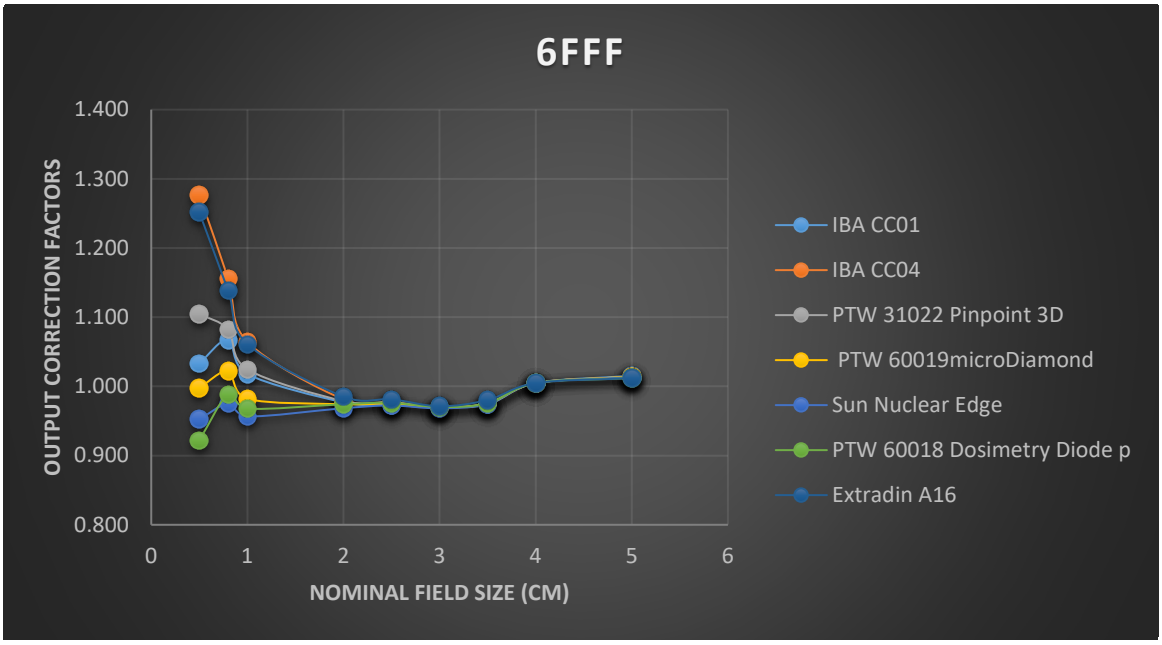

Figure 4.2.2.2 6 FFF photon beam output correction factor plots against field sizes

4.3 T-test statistical analysis and percentage variation

Table 4.3.1 P values obtained as a result of 6 WFF and 6 FFF photon beam comparions for each detector

IBA CC01	0.432
IBA CC04	0.435
Extradin A16	0.100
PTW 31022 Pinpoint 3D	0.252
PTW 60019 micro Diamond	0.181
Sun Nuclear Edge	0.166
PTW 60018 SRS Diode	0.361

Table 4.3.2 Percentage variation of our 6 WFF results from TRS-483 values for each detector

	IBA CC01	IBA CC04	Extradin A16	PTW 31022 Pinpoint 3D	PTW 60019 micro Diamond	Sun Nuclear Edge	PTW 60018 SRS Diode
0.5 cm²	-	-	-	-	-0.2	-	1.4
0.8 cm²	3.4	-	1.6	-	4.1	5.8	6.2
1.0 cm²	3.0	0.4	2.1	-	3.3	4.3	4.5
2.0 cm²	3.8	2.1	2.1	-	2.4	2.5	3.1
2.5 cm²	1.8	0.4	-0.1	-	0.5	0.5	1.2
3.0 cm²	2.1	1.2	0.7	-	1.1	1.1	2.0
3.5 cm²	-	-	-	-	-	-	-
4.0 cm²	0.4	-0.3	-0.3		-0.3	-0.3	0.7
5.0 cm²	-	-	-	-	-	-	-

Table 4.3.3 Percentage variation of our 6 FFF results from TRS-483 values for each detector

	IBA CC01	IBA CC04	Extradin A16	PTW 31022 Pinpoint 3D	PTW 60019 micro Diamond	Sun Nuclear Edge	PTW 60018 SRS Diode
0.5 cm²	-	-	-	-	-3.7	-	3.2
0.8 cm²	-4.0	-	-9.2	-	-4.7	-2.6	-1.7
1.0 cm²	0.0	-2.3	-3.3	-	0.2	0.01	1.5
2.0 cm²	3.1	2.0	1.7	-	2.2	2.5	3.1
2.5 cm²	3.4	2.3	1.9	-	2.4	2.5	3.2
3.0 cm²	3.8	3.0	2.9	-	3.1	3.1	4.1
3.5 cm²	-	-	-	-	-	-	-
4.0 cm²	0.1	-0.6	-0.6		-0.6	-0.6	0.4
5.0 cm²	-	-	-	-	-	-	-

5. DISCUSSION AND CONCLUSION

- In the TRS-483 CoP recommendations (4), it is stated that the output correction factors to be applied in small fields should be between 0.95 and 1.05. In our study, the output correction factors calculated using the Daisy Chain method for both energies as a consequence of the measurements for the field sizes of 1, 2, 2.5, 3, 3.5, 4, and 5 cm^2 were found in the range specified in TRS-483 (4). The correction factors for the ion chamber measurements for the two smallest field sizes, 0.5 and 0.8 cm^2, were found to be greater than 1.05 as expected. This was due to issues such as the LCPE, the partial blocking of the source, perturbation effects, and volume averaging effect, which occurs when field sizes are smaller than 3 cm^2. In the study of Oh et al, it was observed that solid-state detectors should be used instead of ion chambers with field sizes smaller than 3 cm^2 in small field measurements (53). For relative dosimetry, it is also recommended to use detectors whose output correction factors are almost unity like films, scintillations or the detectors, having a low atomic number central electrode. Our results are consistent with the literature (53).

- Tyler et al observed that the detector response in small field measurements is under-response for detectors such as ion chambers since the measurement environment is air and the density of air is lower than the density of water (15). To put it another way, they discovered that bigger correction factors are required. Again, in their study, they found that solid-state detectors such as diamond and silicon diode detectors are over-response because the silicon material is denser than water. In our work, we discovered that ion chambers (IBA CC01, IBA CC04, Standart Imaging Extradin A16, PTW 31022 Pinpoint 3D) was under-response and solid-state detectors (PTW 60019 microDiamond, Sun Nuclear Edge, PTW 60018 SRS Diode) was over-response for the smallest field size (0.5 cm^2). This behavior of detectors is shown in Figure 5.1.a, Figure 5.1.b, Figure 5.2.a, Figure 5.2.b.

The results obtained with PTW 60019 microDiamond detector at a field size of 0.8 cm^2 for 6 FFF energies and IBA CC01 detector at a field size of 0.8 and 1 cm^2 for 6 WFF energies did not match with the findings of Tyler et al.

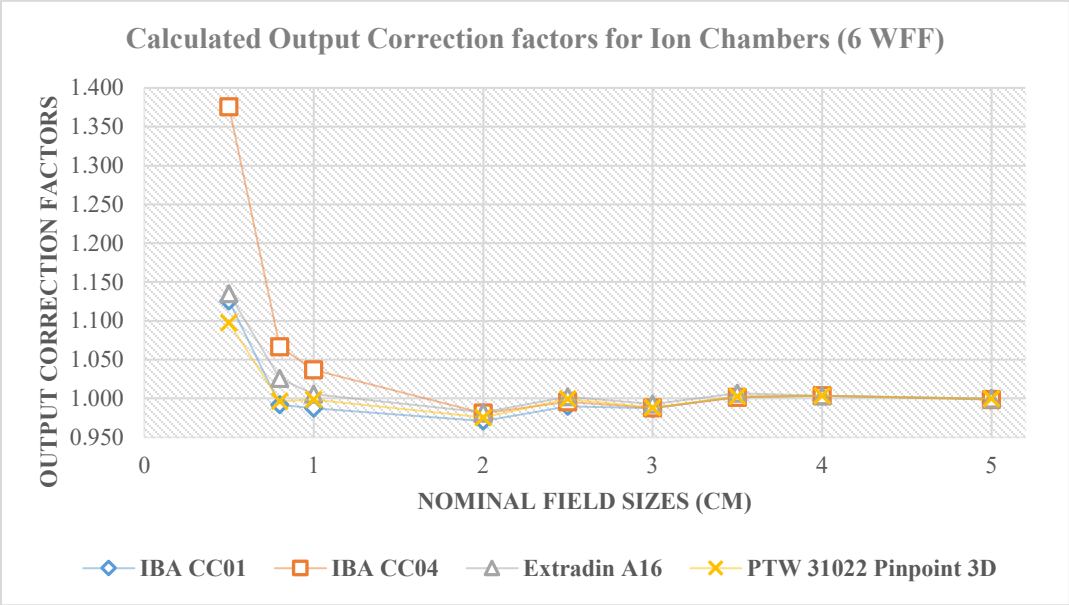

Figure 5.1.a Ion chambers output correction factors at 10 cm depth for 6 WFF

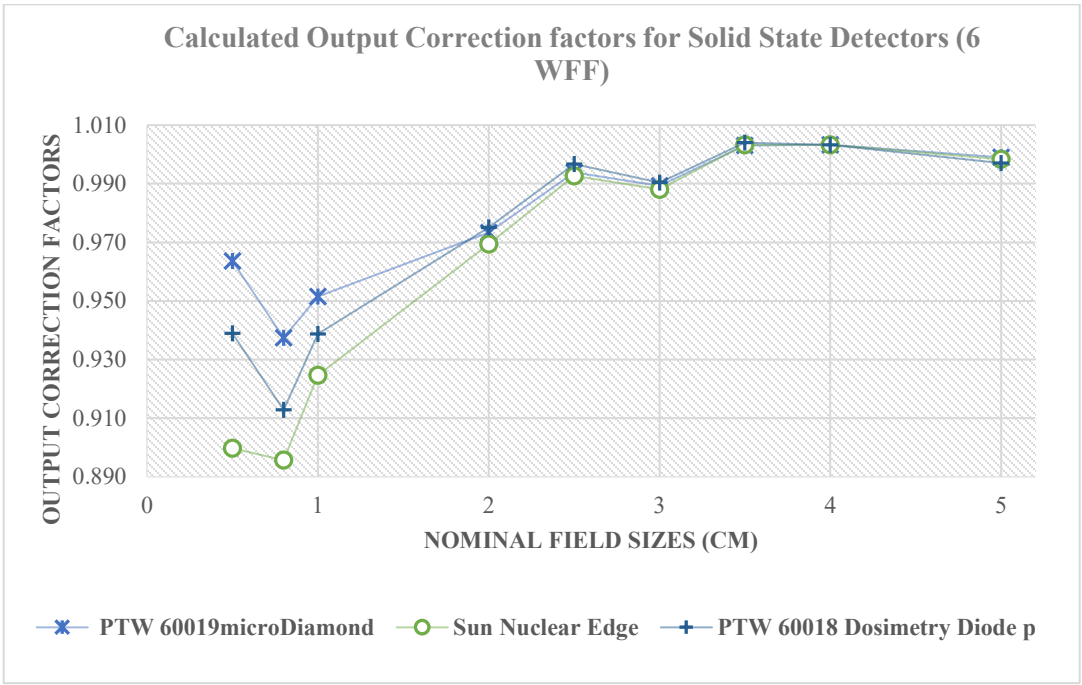

Figure 5.1.b Solid-state detectors output correction factors at 10 cm depth for 6 WFF

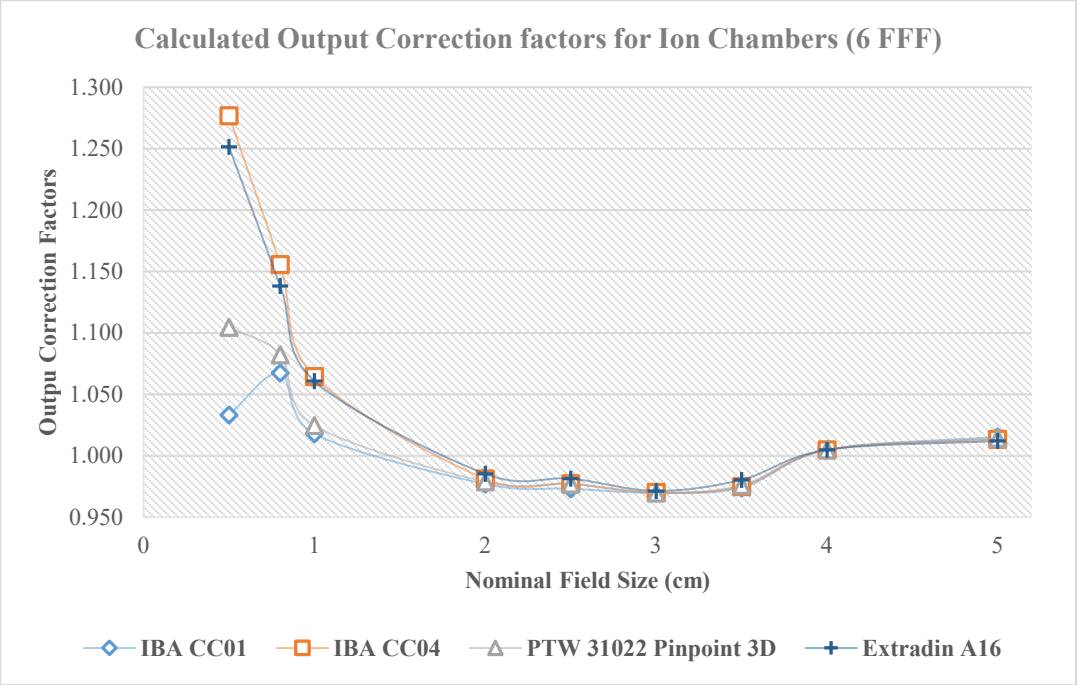

Figure 5.2.a Ion chambers output correction factors at 10 cm depth for 6 FFF

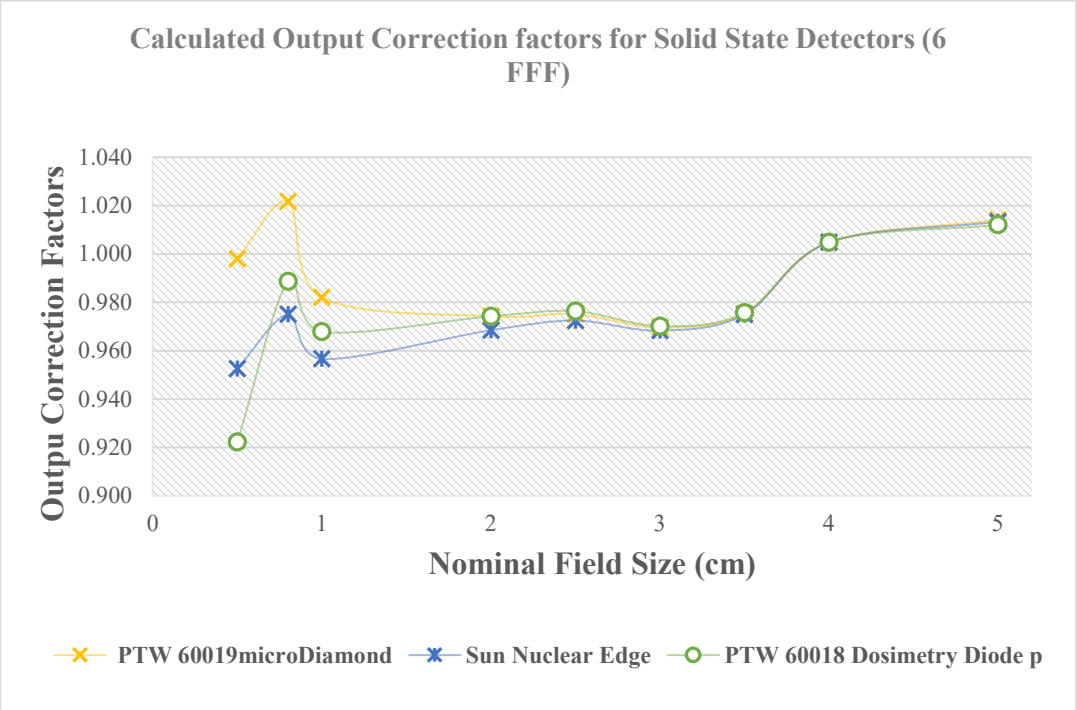

Figure 5.2.b Solid-state detectors output correction factors at 10 cm depth for 6 FFF

- The IBA CC01 was overresponse at 6 wFF among other ion chambers. The SI Extradin A16 detector was under response, but the required correction factor was greater than with other air-filled ion chambers. Both results showed that the volume average effect may be occurred due to the electrode material of these detectors made of steel, thus altering the output factor response of the scattered electrons. Masanga et al found similar results for the smallest field sizes, confirming our observation (54).

- According to Lechner et al study's diamond and unshielded detectors require a smaller correction factor than shielded detectors (55). Cranmer-Sargison et al discovered that shielded detectors increase the dose-response due to the contribution of low energy scattered photons from the shielding resulting with over dose-response and need a bigger correction factor than unshielded detectors (56,57). The results obtained in our study are compatible with these findings for both energies (6 WFF and 6 FFF). In our smallest four field sizes of 0.5, 0.8, 1, and 2 cm^2, we discovered that PTW 60019 microDiamond and PTW 60018 SRS diode (unshielded) detectors require a smaller correction factor than the Sun Nuclear Edge detector for both energies. The correction factor of 0.953 determined for the Sun Nuclear Edge detector at a field size of 0.5 cm^2 for 6 FFF energies is the only exception.

- In our study, the largest output correction factor for our two smallest field sizes, 0.5 and 0.8 cm^2 was calculated for the IBA CC04 ion chamber due to having the largest sensitive volume (0.04 cc) compared to other detectors. For field sizes 0.5 and 0.8 cm^2, it is 1.375 and 1.067 at 6 WFF energies, and 1.277 and 1.156 for 6 FFF energies, respectively.

- According to the findings of Bozidar Casar et al's study, 0.1 percent volume correction should be applied to Elekta Versa HD readings taken with EBT3 film. Since volume correction was not included in our study, the output correction factors we discovered might have a 0.1 percent margin of error (50,8).

- In our study, the values we found for both energies (6 WFF / 6 FFF) for each detector were evaluated by applying the one-tail student test, and $p < 0.05$ was calculated for all detectors, and no statistically significant difference is observed. On the other hand, in the measurements obtained in Tyler et al's study with Elekta device, it's stated that the effect on output correction factors, using filters (WFF) and not using filters (FFF) in all measured field sizes, is between +/- 1% for ion chambers and +/- 1.2% for solid-state detectors (15).

- The percent deviation between the 6 WFF / 6 FFF output correction factors we observed in our study is a maximum of 2% for both ion chambers and solid-state detectors at field sizes of 2 cm^2 and larger. This value is observed at 3% for all detectors except the Extradin A16 detector at 1 cm^2 field size. For our two smallest areas, 0.5 and 0.8 cm^2, the percentage deviation was a maximum of 8%. According to Tylor et al. and our findings, there may be an increase at uncertainty in the correction factors when just one value is used for both energies, as specified in TRS-483.

- Correction factors specified in TRS-483 (4) are specified as a single value independent of the linac device model, collimation system (MLC or jaw), or filter. Again, correction factors for the 0.5, 3.5, and 5.0 cm^2 field sizes and the PTW 31022 Pinpoint 3D ion chamber are not specified in the TRS-483 (4). The study by Dufreneix et al shows that correcting the output factors by taking the correction factors suggested in TRS-483 (4) as reference data and uploading the beam modeling data to TPS in this way will have serious consequences in clinical practice (58). Comparing the correction factors we obtained as a result of our study and the correction factors suggested in TRS-483 (4), it was observed that the percent value deviation for small fields (0.5 and 0.8 cm^2) is above 3.5%. As a result of our study; instead of calculating the output factors by using the correction factors suggested in TRS-483, each clinic's calculation of the detector-specific correction factor for their device and calibration conditions (SSD: 90 and depth: 10 cm) for the detector

available in their clinic will reduce the error encountered in small field dosimetry, and it has been observed that it will be the most correct approach.

- In the study of Bassinet et al., the output correction factor for the Sun Nuclear Edge detector was found to be 0.945 in the Novalis model linac device collimated with a 4 mm circular cone at 6 FFF energy (59). As a result of our study, the field size correction factor of 0.5 cm^2 for the Elekta Versa HD device collimated with Agility 160 MLC and the Sun Nuclear Edge detector is 0.953. This result shows that the linac device model and collimation cause an error of 1% in small fields. The study by Charles et al confirms the findings and shows that the error due to the size of the MLC or jaw-shaped area in small fields (1 cm^2 area size) is reflected in the output data as 3% (60). Results of our experiment and literature reviews show that modeling of TPS data using the correction factors suggested in TRS-483 (4) is not sufficient, and the correction factors calculated as a result of the measurements are also affected by the device and collimation.

- When our findings and the study of Bozidar Casar et al are compared, the deviation from the percentage value for 6 WFF energies varies between 2% and 5.3%, in field sizes less than 2 cm^2 for all detectors we used except IBA CC04 (50, 8). At 6 FFF energy, the deviation from the maximum percentage value was 8.7% in the Sun Nuclear Extradin 16 detector. This result, on the other hand, confirms that the correction factors differ in clinical conditions even if the device and model used and therefore the collimation systems are the same, and confirm our observation that each clinic should calculate the detector-specific correction factors for its device instead of using the correction factors specified in the literature studies.

- In the study of Azangawe et al, the output correction factor for the PTW microDiamond 60019 detector was calculated as 0.961 in the Elekta Precise for 0.6 cm2 field size and 6 WFF Energy (61). The PTW microDiamond 60019 detector correction factor found as a result of our study is 0.964 for 0.5 cm^2 field size in the

Elekta Versa HD. Two different models of linac systems belonging to Elekta company is compatible with each other with a value of % 0.3. The values found by Azangawe et al and at our studies are 1,000 and 0.989, respectively, for 3.0 cm^2 field sizes and the percentage variation is 1.1%.

- In the study of Lio et al, the output correction factor for the PTW 60018 SRS Diode detector was found to be 0.929 at 6 WFF energy for a field size of 0.5 cm^2. The correction factor found as a result of our study is 0.939. The result we found with a variance from 1% is consistent with the literature (58).

- In TRS-483 (4), there is no information about each detector and each field size. As can be seen in Tables 4.3.2 and 4.3.3, the correction factors for the PTW 31022 Pinpoint 3D detector are not specified in TRS-483 (4). Again, output correction factors of IBA CC01, IBA CC04, Extradin A16, and Sun Nuclear Edge detectors for the smallest field size of 0.5 cm^2 and correction factors for all detectors for field sizes of 3.5 to 5 cm^2 are not specified. We contribute to the literature with the results we found.

- Since our study is an experimental method, user-induced errors may be reflected in our results as errors. e.g; in detector effective point detection, possible errors in detector alignment may have occurred in our study as well as in every experimental study, and this difference is observed in some results that are different from the literature. The "A Large Multicentre Study" by Dufreneix et al (58) confirms this observation. Still, The EBT3 gafchromic film dosimeter requires high sensitivity and accuracy. Calibration and dose film measurements, and the film readings we performed with ImageJ software may have been reflected in the output correction factors as uncertainty. Film readings and ROI selections with ImageJ are subject to error as it depends on the the user performing the readings. For this purpose, we have observed that using commercial software developed for this purpose instead of using an open-source resource such as ImageJ for relative dosimeter measurement will reduce the error in output correction factors.

- In our study, correction factors for 7 different detectors and 9 different field sizes (0.5, 1.0, 2.0, 2.5, 3, 3.5, 4.0, 4.5, 5.0 cm^2) were calculated using the experimental method and their compatibility with the correction factors specific to the detectors specified in the literature was investigated. We observed that ion chambers are under-response in field sizes smaller than 3 cm^2 and need a larger correction factor, whereas solid-state detectors are over-response and need a relatively smaller correction factors than ion chambers. The percent variation between the correction factors for the two energies 6 WFF / 6 FFF was found to be a maximum of 2% for both ion chambers and solid detectors at field sizes of 2 cm^2 and larger. We found significant difference between the correction factors for all detectors we used in our study for both energies for the field sizes smaller than 2 cm^2. S_{cp} readings are used to calculate treatment MU values. Dose calculations will be erroneous in treatment plans when small fields such as SRS, SBRT and SRT are commonly used if output correction factors are incorrectly or incompletely supplied owing to detector differences. Although dosimetry systems appropriate for small field output measurements are used, it is beyond the scope of this thesis to indicate which detector is best suited for small field output measurements. More research is needed to support the output correction factor calculation of these detectors and our findings.

6.REFERENCES

1. Ceylan C. Radyoterapide SRS/SBRT uygulamalarında farklı doz fraksiyonlarının ve değişen doz hızlı tedavi tekniklerinin radyobiyolojik etkisi: Farklı hücre kültürleri ile in vitro çalışma. 2019.
2. *IAEA Technical Report Series No.398 Absorbed Dose Determination in External Beam Radiotherapy*.; 2000.
3. Almond PR, Biggs PJ, Coursey BM, et al. AAPM's TG-51 protocol for clinical reference dosimetry of high-energy photon and electron beams. *Med Phys*. 1999;26(9):1847-1870.
4. *Technical Reports Series No.483 Dosimetry of Small Static Fields Used in External Beam Radiotherapy an International Code of Practice for Reference and Relative Dose Determination*.
5. Das IJ, Francescon P, Moran JM, et al. Report of AAPM Task Group 155: Megavoltage photon beam dosimetry in small fields and non-equilibrium conditions. *Med Phys*. 2021.
6. Palmans H, Andreo P, Huq MS, Seuntjens J, Christaki KE, Meghzifene A. Dosimetry of small static fields used in external photon beam radiotherapy: Summary of TRS-483, the IAEA-AAPM international code of practice for reference and relative dose determination. *Med Phys*. 2018;45(11):e1123-e1145.
7. Das IJ, Morales J, Francescon P. Small field dosimetry: What have we learnt? In: *AIP Conference Proceedings*. Vol 1747. American Institute of Physics Inc.; 2016:060001.
8. Casar B, Gershkevitsh E, Mendez I, Jurković S, Saiful Huq M. Output correction factors for small static fields in megavoltage photon beams for seven ionization chambers in two orientations - perpendicular and parallel. *Med Phys*. 2020;47(1):242-259.
9. Beyzadeoglu M, Ozyigit G, Ebruli C. *Basic Radiation Oncology*.; 2010.
10. Bushberg JT, Seibert JA, Leidholdt Jr EM, Boone JM. The Essential Physics of Medical Imaging. *Radiology*. 2012;(3):1048.

11. A.Purdy J, Mutic S. Principles of Radiation Physics and Dosimetry. In: C.Halperin E, E.Wazer D, A.Perez C, W.Brady L, eds. *Perez & Brady's Principles and Practice of Radiation Oncology*. 7th ed. Wolters Kluwer; 2019:546-618.
12. Becerir HB, Alkaya F, eds. *Radyoterapi Fiziği*. 1st ed. Nobel; 2020.
13. Alfred L, Leaver D. Treatment Delivery Equipment. In: Charles M. W, Leaver D, eds. *Principles and Practice of Radiation Therapy*. 4th Editio. Elsevier Ltd; 2016:132-155.
14. Huh H Do, Kim S. History of Radiation Therapy Technology. *Prog Med Phys*. 2020;31(3):124-134.
15. Tyler MK, Liu PZY, Lee C, McKenzie DR, Suchowerska N. Small field detector correction factors: effects of the flattening filter for Elekta and Varian linear accelerators. *J Appl Clin Med Phys*. 2016;17(3):223-235.
16. Podgorsak EB. Treatment Machines For External Beam Radiotherapy. In: Podgorsak EB, ed. *Radiation Oncology Physics: A Handbook for Teachers and Students*. ; :123-160.
17. Khan F, Gibbons JP. *The Physics of Radiation Therapy*. 5th ed. Minnesota: Lippincott Williams & Wilkins; 2014.
18. Schlegel W, Bortfeld T, Grosu A-L. Beam Delivery in 3D Conformal Radiotherapy Using Multi-Leaf Collimators. In: Brady LW, Heilmann H-P, Molls M, eds. *New Technologies in Radiation Oncology*. Berlin, Heidelberg; 2006:257-266.
19. Cho B. Intensity-modulated radiation therapy: A review with a physics perspective. *Radiat Oncol J*. 2018;36(1):1-10.
20. Sveistrup J, af Rosenschöld PM, Deasy JO, et al. Improvement in toxicity in high risk prostate cancer patients treated with image-guided intensity-modulated radiotherapy compared to 3D conformal radiotherapy without daily image guidance. *Radiat Oncol*. 2014;9(1).
21. Nill S, Hinderer R, Oelfke U. X-IMRT. In: Brady LW, Heilmann H-P, Molls M, eds. *New Technologies in Radiation Oncology*. 4th ed. ; 2016:289-298.
22. Prado CM, Prado KL. Photon Dose Distributions. In: Washington CM, Leaver D, eds. *Principles and Practice of Radiation Therapy*. 4th ed. ; 2016:523.
23. Brian L, Leaver D. Medical Imaging. In: Charles M. W, Leaver D, eds. *Principles and Practice of Radiation Therapy*. 4th ed. Elsevier Inc.; 2016:126.

24. T.Gillin M. Special Procedures. In: Charles M. Washington, Leaver D, eds. *Principles and Practice of Radiation Therapy*. 4th ed. Elsevier Ltd; 2016:310-322.
25. Grosu A-L, Kneschaurek P, Schlegel W. Stereotactic Radiotherapy/Radiosurgery. In: Brady LW, Heilmann H-P, Molls M, eds. *New Technologies in Radiation Oncology*. ; 2006:267-276.
26. Herfarth KK. Extracranial Stereotactic Radiation Oncology. In: L. W. Brady, Heilmann H-P, Molls M, eds. *New Technologies in Radiation Oncology*. Springer; 2006:277-288.
27. Benedict SH, Yenice KM, Followill D, et al. Stereotactic body radiation therapy: The report of AAPM Task Group 101. *Med Phys*. 2010;37(8):4078-4101.
28. Kim Y, Setiniyaz S, Titberidze M, Jang KH. Overall performance comparison of S-band C-band, and X-band based compact XFEL facilities. *FEL 2012 - 34th Int Free Electron Laser Conf*. 2012:149-152.
29. Yu C, Main W, Taylor D, et al. An anthropomorphic phantom study of the accuracy of CyberKnife spinal radiosurgery. *Neurosurgery*. 2004;55(5):1138-1146.
30. Goer DA, Musslewhite CW, Jablons DM. Potential of mobile intraoperative radiotherapy technology. *Surg Oncol Clin N Am*. 2003;12(4):943-954.
31. Snyder KC, Wen N. Linac-Based SRS/SBRT Dosimetry. In: Darafsheh A, ed. *Radiation Therapy Dosimetry A Practical Handbook*. Taylor & Francis; 2021:277-303.
32. Georg D, Knöös T, McClean B. Current status and future perspective of flattening filter free photon beams. *Med Phys*. 2011;38(3):1280-1293.
33. Klein EE, Hanley J, Bayouth J, et al. Task group 142 report: Quality assurance of medical acceleratorsa. *Med Phys*. 2009;36(9):4197-4212.
34. *ICRU Report 91. Prescribing Recording, and Reporting of Stereotactic Treatments with Small Photon Beams.*; 2017.
35. Andreo P. An introduction to IAEA TRS-483. 2018.
36. Sharpe MB, Miller BM, Yan D, Wong JW. Monitor unit settings for intensity modulated beams delivered using a step-and-shoot approach. *Med Phys*. 2000;27(12):2719-2725.

37. Alfonso R, Andreo P, Capote R, et al. A new formalism for reference dosimetry of small and nonstandard fields. *Med Phys*. 2008;35(11):5179-5186.
38. 2. Small Field Dosimetry. *J Int Comm Radiat Units Meas*. 2014;14(2):31-53.
39. Setilo I, Oderinde OM, Plessis FC Du. The effect of SSD, Field size, Energy and Detector type for Relative Output Factor measurement in small photon beams as compared with Monte Carlo simulation. *Polish J Med Phys Eng*. 2019;25(2):101-110.
40. Huet C, Moignier C, Fontaine J, Clairand I. Characterization of the gafchromic EBT3 films for dose distribution measurements in stereotactic radiotherapy. *Radiat Meas*. 2014;71:364-368.
41. Niroomand-Rad A, Blackwell CR, Coursey BM, et al. Radiochromic film dosimetry: Recommendations of AAPM Radiation Therapy Committee Task Group 55. *Med Phys*. 1998;25(11):2093-2115.
42. Chand B, Kumar M, Kumar M. Comprehensive Review Of Small Field Dosimetry. *Eur J Mol Clin Med*. 2020;7(7):3595-3607.
43. Chianese J, Chamberlain F. Radiation Dosimetry. In: Cherry P, M.Duxburry A, eds. *Practical Radiotherapy Physics & Equipment*. Second. Wiley-Blackwell; 2009:25-35.
44. Cho W, Kim S, Kim J-I, et al. Dosimetric effects on small-field beam-modeling for stereotactic body radiation therapy. *J Korean Phys Soc*. 2015;66(4):678-693.
45. Lechner W, Primeßnig A, Nenoff L, Wesolowska P, Izewska J, Georg D. The influence of errors in small field dosimetry on the dosimetric accuracy of treatment plans. *Acta Oncol (Madr)*. 2020;59(5):511-517.
46. Ahnesjö A, Weber L, Murman A, Saxner M, Thorslund I, Traneus E. Beam modeling and verification of a photon beam multisource model. *Med Phys*. 2005;32(6):1722-1737.
47. Oelfke U, Scholz C. Dose Calculation Algorithms. In: Brady LW, Heilmann H-P, Molls M, eds. *New Technologies in Radiation Oncology*. Springer Berlin Heidelberg; :187-196.
48. Ahnesjö A. Small Field Dosimetry: Beam and dose modelling in TPS. In: *2013 AAPM Annual Meeting Anders Ahnesjo, PhD, Uppsala University, SWEDEN*. ; 2013. https://vimeo.com/76977496.

49. IBA. *Detectors for Relative and Absolute Dosimetry*. IBA; 2013. www.iba-dosimetry.com.
50. Casar B, Gershkevitsh E, Mendez I, Jurković S, Huq MS. A novel method for the determination of field output factors and output correction factors for small static fields for six diodes and a microdiamond detector in megavoltage photon beams. *Med Phys*. 2019;46(2):944-963.
51. Howard ME, Herman MG, Grams MP. Methodology for radiochromic film analysis using FilmQA Pro and ImageJ. *PLoS One*. 2020;15(5):1-12.
52. Méndez I, Rovira-Escutia JJ, Casar B. A protocol for accurate radiochromic film dosimetry using Radiochromic.com. *Radiol Oncol*. 2021;55(3):369-378.
53. Oh SA, Yea JW, Lee R, Park HB, Kim SK. Dosimetric Verifications of the Output Factors in the Small Field Less Than 3 cm 2 Using the Gafchromic EBT2 Films and the Various Detectors . *Prog Med Phys*. 2014;25(4):218.
54. Masanga W, Tangboonduangjit P, Khamfongkhruea C, Tannanonta C. Determination of small field output factors in 6 and 10 MV flattening filter free photon beams using various detectors. *J Phys Conf Ser*. 2016;694(1).
55. Lechner W, Palmans H, Sölkner L, Grochowska P, Georg D. Detector comparison for small field output factor measurements in flattening filter free photon beams. *Radiother Oncol*. 2013;109(3):356-360.
56. Cranmer-Sargison G, Weston S, Sidhu NP, Thwaites DI. Experimental small field 6 MV output ratio analysis for various diode detector and accelerator combinations. *Radiother Oncol*. 2011;100(3):429-435.
57. Cranmer-Sargison G, Charles PH, Trapp J V., Thwaites DI. A methodological approach to reporting corrected small field relative outputs. *Radiother Oncol*. 2013;109(3):350-355.
58. Dufreneix S, Bellec J, Josset S, Vieillevigne L. Field output factors for small fields: A large multicentre study. *Phys Medica*. 2021;81(July 2020):191-196.
59. Bassinet C, Huet C, Derreumaux S, et al. Small fields output factors measurements and correction factors determination for several detectors for a CyberKnife® and linear accelerators equipped with microMLC and circular cones. *Med Phys*. 2013;40(7).

60. Charles PH, Cranmer-Sargison G, Thwaites DI, et al. A practical and theoretical definition of very small field size for radiotherapy output factor measurements. *Med Phys*. 2014;41(4):041707.
61. Azangwe G, Grochowska P, Georg D, et al. Detector to detector corrections: a comprehensive experimental study of detector specific correction factors for beam output measurements for small radiotherapy beams. *Med Phys*. 2014;41(7).

7. CURRICULUM VITAE

Personal Informations

Name	Burcu	**Surname**	Hız Temizer
Place of Birth		**Date of Birth**	
Nationality		**TR ID Number**	
E-mail		**Phone number**	

Education

Degree	Department	The name of the Institution Graduated From	Graduation year
Doctorate	-	-	-
Master	Yeditepe University	**Medical Physics**	2021
University	Istanbul Technical University	**Physics Engineering**	1999
High school	Besiktas High School	**Mathematics**	1994

Languages	**Grades (#)**
English	Yökdil (81.250)
German	

All the grades must be listed if there is more than one (KPDS, ÜDS, TOEFL; İELTS vs),

Work Experience (Sort from present to past)

Position	**Institute**	**Duration (Year - Year)**
Business Unit Manager	Toshiba Medical Systems	2008-2017
Modality Sales Specialist	GE Healthcare	2007-2008
Product Manager	Toshiba Medical Systems	2002-2007

Computer Skills

Program	**Level**
MS (Excel, Word, Powerpoint)	Good

***Excellent , good, average or basic**

Others (Projects / Certificates / Rewards)

National Medical Physics Congress (04 - 07 Nov 2021) Oral Presentation